D1.3 – Report on kinetic mechanisms and radiation modelling

Christian Schwenzer, Heinz Pitsch, Huanhuan Xu, Joachim Beeckmann, Miguel Buenaflor, Raymond Langer, and Sanket Girhe

| RWTH Aachen University – ITV

Alex Garcia Vergara, Johannes Losacker, and Nico Schmitz | RWTH Aachen University – IOB

Daniel Mira and Eduardo Pérez

| Barcelona Supercomputing Center

December 2023

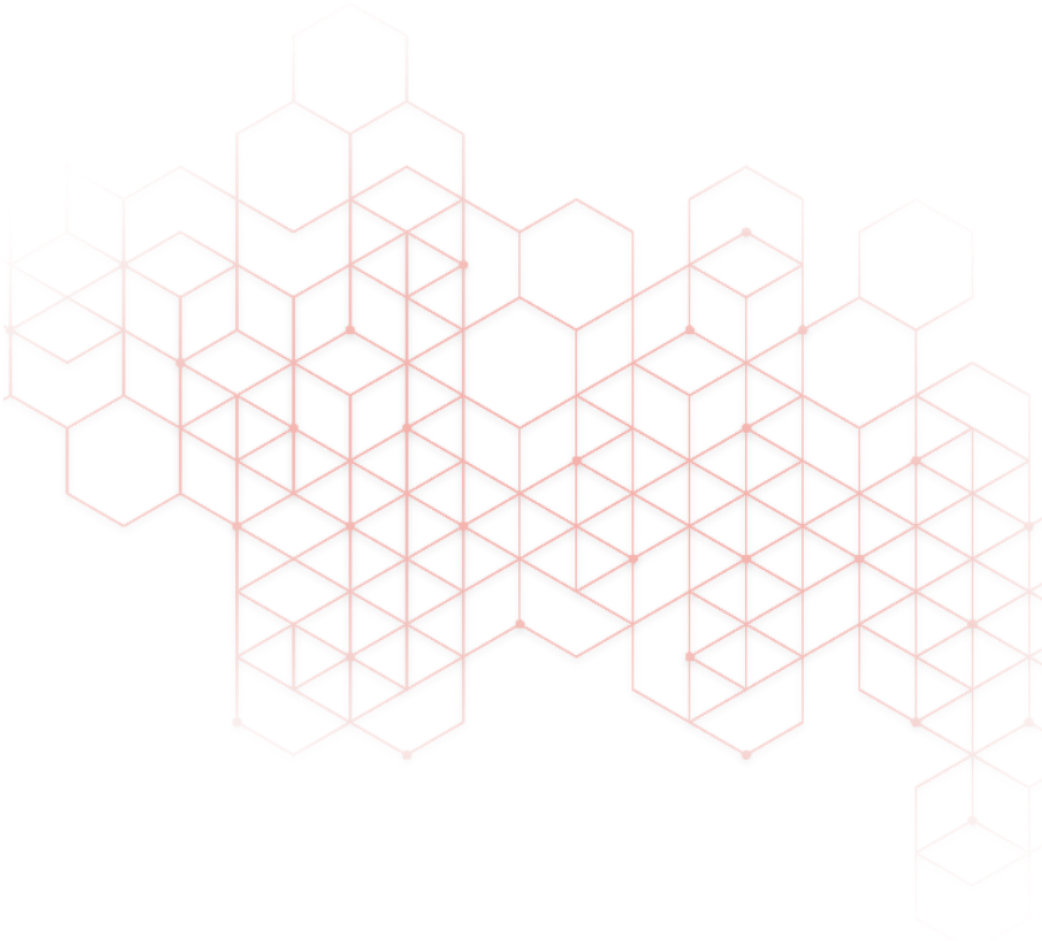

Credits

Disclaimer

This project has received funding from the European Union's Horizon Europe research and innovation programme under grant agreement No 101091456.

Technical references

Grant Agreement N°	101091456	Acronym	HyInHeat
Full Title	D1.3 - Report on kinetic mechanisms and radiation modelling		
Work Package (WP)	WP1		
Authors	Alex Garcia Vergara, Christian Schwenzer, Daniel Mira, Eduardo Pérez, Heinz Pitsch, Huanhuan Xu, Joachim Beeckmann, Johannes Losacker, Miguel Buenaflor, Nico Schmitz, Raymond Langer, and Sanket Girhe		
Leading organisation	RWTH Aachen University		
Date of publication	21/12/2023		
Contributors	Franziska Ott		
Document Type	R – Document, report		
Document Title	Report on kinetic mechanisms and radiation modelling		
Dissemination Level (delete unnecessary options)	Public		

Document history

Version	Date	Partner	Author
1	31/08/2023	BSC	Daniel Mira and Eduardo Pérez
2	06/09/2023	RWTH-ITV	Christian Schwenzer, Huanhuan Xu, and Joachim Beeckmann
3	08/09/2023	RWTH-IOB	Alex Garcia Vergara and Johannes Losacker
4	21/09/2023	BSC, RWTH-IOB	Alex Garcia Vergara, Eduardo Pérez, and Johannes Losacker
5	28/09/2023	RWTH-ITV	Huanhuan Xu, Joachim Beeckmann, Miguel Buenaflor, Raymond Langer, and Sanket Girhe
Final	21/12/2023	RWTH-ITV, RWTH-IOB, BSC	Alex Garcia Vergara, Christian Schwenzer, Eduardo Pérez, Heinz Pitsch, Huanhuan Xu, Joachim Beeckmann, Johannes Losacker, Miguel Buenaflor, and Nico Schmitz

Contents

Tables & Figures

List of abbreviations

Abbreviations	Explanation
ATI	Average time per iteration
BB	Bunsen burner
CFD	Computational fluid dynamics
DOM	Discrete ordinates method
FVM	Finite volume method
LBL	Line-by-Line
LBV	Laminar burning velocity
LES	Large eddy simulations
LM	Linear method
MC	Monte Carlo
NM	Non-linear method
OTA	Optical thin assumption
PAH	Polycyclic aromatic hydrocarbon
RANS	Reynolds averaged Navier-Stokes
RMSE	Relative root mean squared error
RTE	Radiative transfer equation
SEF	Spherically expanding flame
SLW	Spectral-Line-Based WSGGM
WSGGM	Weighted-sum-of-gray-gases model

1 Executive Summary

This report deals with updating the kinetic mechanism for H_2/O_2 combustion and extending radiation models suitable for high H_2O content furnace atmospheres. Deliverable 1.3 is a summary of the work carried out in Task 1.4 of HyInHeat project. The mechanism scheme and radiation models from this report will be used for the development of efficient simulation platforms in Task 2.3 of HyInHeat, and this efficient simulation platform will be used to perform both Reynolds averaged Navier-Stokes (RANS) and Large Eddy Simulations (LES) for turbulent H_2/O_2 and H_2/air flames for real application environments.

The present document is subdivided into two parts. Part I deals with the validation of the H_2/O_2 combustion kinetic mechanisms, while part II focuses on radiation modelling and heat transfer for engineering (by performing RANS) and high-fidelity simulations (by applying LES). Outlines for these two parts are given below.

Part I: H_2/O_2 combustion kinetics

The motivation and necessity of H_2/O_2 combustion mechanism development is first introduced. Laminar Burning Velocity (LBV) [1] can be used for kinetic mechanism validation. Aiming at an H_2/O_2 combustion environment, available LBV measurements and state-of-the-art chemical kinetic mechanisms are presented. Then the experimental and simulation methods for LBV are introduced, and following this, the experiments and simulation results under broad combustion conditions are analysed and discussed. Based on a comparison of simulation results and measurements, a suitable mechanism for H_2/O_2 combustion is suggested in closing.

Part II: Radiation modelling and heat transfer for engineering (RANS) and high-fidelity (LES) simulations

In this part, thermal radiation modelling is reviewed. The most used modelling approaches for the radiation heat transfer equation and the gas absorptivity are assessed in order to find a suitable model to describe thermal radiation in high-temperature processes with natural gas–hydrogen mixtures and oxyfuel combustion. One of the goals is to define the most appropriate model to be implemented in Alya [2], the multi-physics code developed at the Barcelona Supercomputing Center, to perform the LES simulations. The decision is based on the literature review and the results from evaluating various models in RANS simulations of a high-temperature combustion system based on a lab-scale furnace available at the IOB laboratory at RWTH Aachen University.

Objectives and subtasks

This report aims to provide an updated chemical kinetic mechanism and gas radiation models for H_2/O_2 turbulent combustion simulations at lab-scale and industrial process levels. To this end, the following subtasks are fulfilled:

- Measure laminar burning velocities
- Obtain combustion instability maps
- Establish an updated kinetic scheme
- Revise approaches in the RANS framework: to allow efficient simulation of radiative heat transfer
- Extend radiation models to be used in the LES framework
- Evaluate the prediction quality of radiation models and computational effort

2 H_2/O_2 Combustion Kinetic Mechanisms

2.1 Introduction

Due to its multiple advantages like carbon-free, cleanliness, renewability, high heating value per mass unit, and high energy efficiency, hydrogen has become one of the most promising fuels for decarbonizing industrial combustion. However, utilizing hydrogen also comes with some challenges such as a lack of flame stability, the possibility of flashbacks, high flame temperatures, and high NO_x emission levels. Effectively addressing these challenges and precisely predicting the described phenomena in practical application requires an accurate combustion mechanism for H_2/O_2.

2.1.1 Background

As summarized in the extensive literature, hydrogen combustion differs greatly from conventional hydrocarbon fuels. For instance, the level of adiabatic flame temperature is around 150 K higher compared to CH_4 and C_3H_8 with the same stoichiometry. The increasing adiabatic flame temperatures associated with higher H_2 contents in fuel mixtures may lead to higher thermal NO_x emissions. A highly efficient and environment-friendly utilization of H_2 in industrial heating application appears to be oxy-combustion, where the fuel or oxidant flows are diluted with a large amount of exhaust gas. Reducing N_2 content or excluding N_2 from the combustion process decreases NO_x emissions. In addition, oxy-combustion is beneficial in fuel saving and capacity increasing [3]. Eliminating the nitrogen from the oxidizing mixture decreases the flue gas volume significantly, decreasing the heat loss from the flue gas. As hydrogen gains increasing attention as a clean energy carrier, oxy-combustion emerges as a promising approach to maximize its benefits across various industrial sectors while minimizing environmental impacts.

2.1.1.1 Kinetic mechanism development

Efficiently developing clean combustion technologies for hydrogen benefits from Computational Fluid Dynamics (CFD), which is very important to evaluate the safety of both facilities and operators and to optimize H_2 combustion performance. Particularly, CFD models depend on accurate H_2/O_2 kinetic mechanisms to model high-temperature chemical processes. However, as H_2 oxy-combustion involves higher temperatures than air combustion, existing air-combustion kinetics may not apply accurately. Discrepancies in reaction pathways, rate constants, and third-body effects can undermine predictive performance. To enhance modelling accuracy, an updated kinetic mechanism is essential to address uncertainties in rate coefficients and missing reactions in the context of hydrogen combustion.

The rapid development of fuels' chemical kinetic mechanisms has been witnessed in the past several decades. A number of mechanisms were proposed for H_2 combustion, also. Owing to the satisfactory kinetic database for H_2/air combustion, the optimization of mechanisms is a viable method for developing a better combustion model for O_2-enriched environments. Mechanism optimization is a process that involves a systematic search of parameter values of the combustion model to achieve the best possible reproduction of a selected set of experimental results. In most studies, rate parameters are modified in this way. In principle, thermodynamic and transport parameters can also be included in an optimization task, but changing the values of these parameters within their uncertainty ranges usually has a much smaller effect on simulation results than the rate parameters itself.

Regarding the experimental data for kinetic mechanism validation, comprehensive experimental data were either measured or collected from literature, including laminar burning velocity, ignition delay times, and species concentration profiles. These types of experimental data, called indirect measurements or bulk measurements, have been widely used to validate detailed reaction mechanisms.

2.1.2 State of the art

Laminar Burning Velocity (LBV) as a fundamental flame metric is of particular importance since it provides information on the overall reactivity and can be used to constrain uncertainties of chemical models or as a scaling factor in turbulent combustion models [1]. In some literature, LBV is alternatively referred to as laminar flame speed. The experimental methodologies for fundamental flame speed determination involve flames that are either stationary, including conical, flat, and counter-flow flames or they are propagating with

respect to a quiescent unburned mixture like Spherically Expanding Flames (SEF) [4]. Out of these methodologies, the SEF, either as a dual chamber concept with fixed pressure or as a single chamber concept, offers flexibility in terms of varying initial pressures, temperatures, and gas compositions [5].

2.1.2.1 Availability of LBV measurements for $H_2/O_2/N_2$ mixtures

The availability of H_2 LBV burning in different O_2-containing oxidizers is reviewed to understand the state-of-the-art. Table 2- 1 lists the existing measurements for LBV of H_2 burning in pure oxygen. Dixon-Lewis et al. [6] measured the LBV of H_2/O_2 mixtures using SEF method. Experiments were conducted at 1 bar and a wide range of equivalence ratio from 0.85 to 5.3 was investigated. Zitoun et al. [7] studied LBV of rich H_2/O_2 mixtures, with a focus of the impact of initial temperature on LBV. Due to inaccuracies caused by compression effects and exceptionally high expansion ratios at low temperatures (100 K to 300K), Bunsen Burner (BB) method was employed. Jahn et al. [8] and Warnatz et al. [9] also used the BB method to measure LVB of H_2/O_2 mixtures. Clearly, these data are very scarce, and most are out of date. Considering their uncertainties might be not comparable to the recent experiments', measurements with high reliability are required.

Table 2- 1 Summary of literature data of H_2 LBV burning with pure O_2.

Author	Fuel	Method	x_{O_2}	Φ	p (bar)	T (K)
Chen et al.[10] (2022)	H_2	SEF[1]	100%	0.5, 0.8, 1.0,1.5/ 0.8, 1.0, 1.5/1.5;	0.1,0.3,0.5/1/1.2,1.5;	298
Dixon-Lewis et al. [6] (1984)	H_2	SEF	100%	0.85, 1.30, 1.68, 2.23, 3.20, 5.30	1	293
Zitoun et al. [7] (1997)	H_2	BB[2]	100%	1,2,3,4,5	1	293
Jahn et al. [8] (1934)	H_2	BB	100%	1,2,3,4,5	1	293
Warnatz et al. [9] (1979)	H_2	BB	100%	1,2,3,4,5	1	293

[1] SEF: Spherically expanding flame
[2] BB: Bunsen burner

H_2 LBVs under O_2-enriched environment and air environment are summarized in Table 2- 2 and Table 2- 3, respectively. Yang et al. [11] measured the LBV of H_2/O_2 mixtures with equivalence ratios ranging from 0.3 to 2.5 at initial pressures of 0.25 to 1 bar. It is worth noting that although this investigation studied the influence of O_2 content (from 24.4% to 48.78%), they introduced either He or CO_2 as a diluent, which is different from the combustion environment concerned in Task 1.4, namely the oxidizer of O_2 and N_2. Compared with pure O_2 and O_2-enriched conditions, measurements under air-combustion are quite abundant.

Table 2- 2 Summary of literature data of H_2 LBV under O_2-enriched environment.

Author	Fuel	Method	x_{O_2}	Φ	p (bar)	T (K)
Yang et al. [11] (2017)	H_2	SEF	48.7%	2.5	0.25, 0.38, 0.50, 0.62, 0.75, 0.87, 1	295
Yang et al. [11] (2017)	H_2	SEF	38.6%	2.5	0.25, 0.38, 0.50, 0.62, 0.75, 0.87, 1	295
Yang et al. [11] (2017)	H_2	SEF	38.17%	0.3	0.25, 0.38, 0.50, 0.62, 0.75, 0.87, 1	295
Yang et al. [11] (2017)	H_2	SEF	25%	0.3	0.25, 0.38, 0.50, 0.62, 0.75, 0.87, 1	295
Yang et al. [11] (2017)	H_2	SEF	24.4%	0.3	0.35, 0.38, 0.45, 0.50, 0.55, 0.58, 0.67, 0.75, 0.87, 1	295
Yang et al. [11] (2017)	H_2	SEF	100%	0.3	0.25, 0.31 0.38, 0.44, 0.50, 0.62, 0.75, 0.87, 1	295

Table 2- 3 Summary of literature data of H_2 LBV burning in air.

Author	Fuel	Method	x_{O_2}	Φ	p (bar)	T (K)
Alekseev[12] (2015)	H_2	SEF	21%	0.4-0.5	1	298
Dayma [13] (2014)	H_2	SEF	21%	0.5/1/1.7/3/0.5-4	0.2-2/ 0.2-1.3/0.2-1.7/0.3-3/1	303
Krejci [14] (2013)	H_2	SEF	21%	0.5-5	1, 5, 10	298
Kuznetsov [15] (2012)	H_2	SEF	21%	0.25-2/1/2	1/0.2-1/0.2-1	298
Hu [16] (2009)	H_2	SEF	21%	0.6-4.5	1	303
Burke [17] (2009)	H_2	SEF	21%	0.6-5.5	1	298
Over 20 Authors	H_2	SEF	21%	0.2-7	0.2-3	295-303

There is only one recent study regarding H_2 LBV burning with pure O_2. Other available data are out of date and less reliable to be used for the mechanism validation. One reason behind this is that at large O_2 content, flame temperature is enhanced, flame stability is weakened, and flame propagates faster, and all these changes cause significant challenges for the measurements. It can be seen that under air combustion condition, a wide range of equivalence ratios has been measured and the initial pressure varies from 0.2 to 10 bar. Data are available under quite broad combustion conditions for air-combustion. However, as O_2 content increases, LBV measurements were only conducted either for a mixture with an equivalence ratio away from the stoichiometry or under a lower initial pressure.

Figure 2- 1 explicitly displays a number of reported measurements under different equivalence ratios and O_2 content. Again, data for air-combustion are abundant compared to the O_2-enriched and O_2-reduced combustion, and this phenomenon is more apparent when eliminating old data prior to 2000, as shown in Figure 2- 2. H_2 LBV measurements with high O_2 content are extremely limited, and some of them were not measured using SEF method. H_2/O_2 flames exhibit high stretch-ability and strong non-equilibrium characteristics. Any flame configuration used for LBV measurement should subject the flame to a well-defined stretch rate, i.e., a rate that is uniformly distributed over the surface associated with the LBV. Specifically, SEF method offers distinct advantages over alternative methodologies due to its simple flame configuration, well-defined flame stretch rate, and flexibility in accommodating various initial conditions.

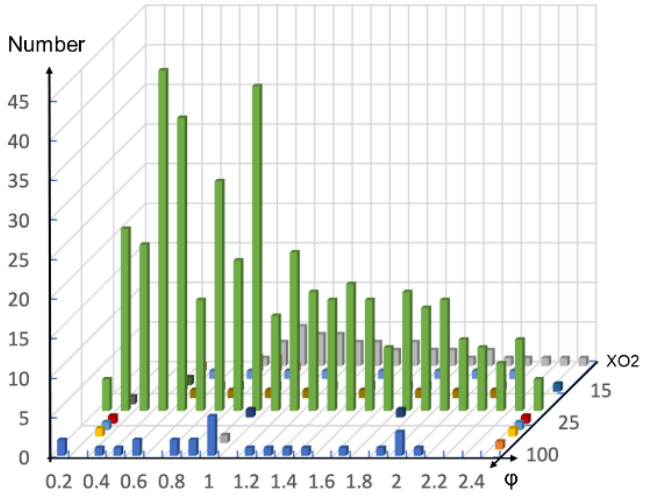

Figure 2- 1 Existing data as function of Φ and xO_2

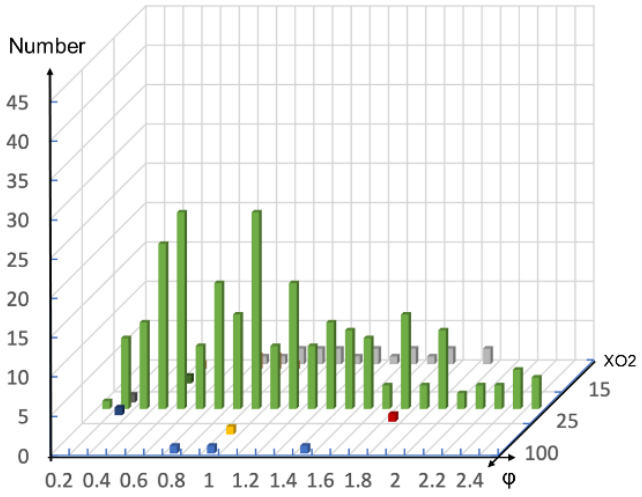

Figure 2- 2 Existing data as function of Φ and xO_2 with modifications (data prior to 2000 are neglected)

2.1.2.2 Availability of H_2/O_2 combustion mechanisms

Various kinetic mechanisms for the numerical investigation of H_2/O_2 combustion already exist in the literature. These range from pure hydrogen mechanisms to detailed kinetic mechanisms, which include, apart from the hydrogen-related kinetics, various other gaseous and liquid fuels. Such detailed mechanisms may be used to describe fuel blends consisting of carbon monoxide, methane, ammonia, and hydrogen. The overarching aim is the evaluation of recent kinetic mechanisms based on experimental laminar burning velocity data for H_2/O_2 obtained in this project and also found in literature. Additionally, a suitable detailed kinetics mechanism for H_2/O_2 combustion should additionally be able to describe mixtures with methane (CH_4) and/or ammonia (NH_3).

The development of recently published kinetic mechanisms is predominantly based on already existing base mechanisms from literature. Two frequently used base mechanisms are Hong et al. [18] and Burke et al. [19] . Hong et al. [18] have developed an optimized hydrogen mechanism that incorporates updated reaction rates from measurements of shock tube experiments, resulting in improved rates, particularly for high temperatures. The mechanism has been validated against a wide range of experimental data, including ignition delay times, speciation measurements from flow reactors and flames, and laminar burning velocities [18]. The kinetic mechanism for hydrogen developed by Burke et al. [19] has also been validated using a wide range of experiments. The main focus in developing this mechanism was to minimize the discrepancy between simulation and experiments using existing mechanisms describing flames especially at dilute mixtures and high pressures [19].

In addition, the less recent but still commonly used GRI-Mech 3.0 mechanism [20] is considered in this work. This mechanism was developed for natural gas combustion and includes hydrogen kinetics. The mechanism was optimized to accurately predict various combustion properties.

The two most recent available detailed mechanisms, mechanism of Langer et al. (referred to ITV mechanism below) [21] and mechanism from Galway (NUIG mechanism, to be officially published), were built on the work of Burke et al. [19] . In particular, ITV mechanism is mainly based on Burke et al. [19], whereas NUIG is from both Hong et al. [18] and Burke et al. [19].

However, these base mechanisms can also be found in other mechanisms such as those of Sun et al. [22], CRECK [23], and SanDiego [24] in terms of hydrogen kinetics, which can be used to describe the combustion of Syngas. In this context, special attention should be drawn to the mechanism by Varga et al. [25], as it is the most recent optimized mechanism regarding H_2/Syngas kinetics. Further kinetic models in that regard are listed in Table 2- 4 .

NUIG mechanism, a detailed kinetic model developed for combustion kinetics of several surrogate fuels, was extensively validated over laminar burning velocities and ignition delay times of pure H_2 as well as several blends including H_2/CO, H_2/CH_4, H_2/CH_3OH, H_2/NH_3 over a broad range of conditions. For H_2, burning

velocities were validated for a wide spectrum of conditions, such as pressures spanning from 1 to 20 atm, equivalence ratios ranging from 0.2 to 5 and a temperature of 298 K. Ignition delay times were validated against both high-temperature data obtained from shock tube experiments and low-temperature data measured in a rapid compression machine. The conditions encompassed temperatures from 877 K to 2000 K, pressures ranging from 1 to 250 atm, and equivalence ratios between 0.1 and 2.

The ITV mechanism is a detailed chemical kinetic model for Polycyclic Aromatic Hydrocarbon (PAH) chemistry that builds on a chemical kinetic mechanism for gasoline surrogates by Langer et al.[21]. Informed by ab initio and experimental studies, the mechanism development emphasizes the prediction of soot precursors starting from C_3H_4 isomers up to the size of acepyrene. The ITV mechanism was validated against experimental measurements from 79 publications, including ignition delay times, laminar burning velocities, and speciation data for several fuels in various conditions. In addition, since the ITV mechanism includes the H_2/O_2 kinetic mechanism developed by Burke et al. [19], the predictions for hydrogen combustion are expected to be broadly consistent. The Burke mechanism [19] is validated against a wide range of experimental conditions, including those found in shock tubes, flow reactors, and laminar premixed flame.

Table 2- 4 Mechanism literature review.

Name	Year	Ref.	Species	Reactions	H_2	CH_4	NH_3	CO
GRI-Mech 3.0	1999	[20]	14	52	X	(X[6])	-	-
Hong et al.	2011	[18]	10	62	X	-	-	-
Burke et al.	2011	[19]	13	54	X	-	-	-
NUIG	2023	[-][1]	11	58	X	(X)	(X)	(X)
ITV	2022	[21]	13	56	X	(X)	(X)	(X)
SanDiego	2016	[24][2]	57	268	X	X	-	X
Konnov	2019	[26][3]	15	150	X	-	-	-
CRECK (Syngas)	2020	[23]	21	116	X	-	-	X
Mei et al.	2021	[27]	34	477	X	-	X	-
Sun et al.	2022	[28]	44	525	X	-	-	x
NUIG 1.1	2020	[29]	16	80	X	(X)	(X)	(X)
NUIG 1.3	2023	[-][5]	9	56				

[1] Last kinetic mechanism regarding H_2-chemistry (to be officially published)
[2] Further literature: Sánchez et al., 2014 [30]
[3] Further literature: Konnov, 2015 [31]
[4] Both NUIG 1.1 & C3 [32] have identical H_2-chemistry
[5] Further developed kinetic mechanism of NUIG 1.3 (not officially published)
[6] Not available

2.2 Methodology and procedures

2.2.1 Experimental method for laminar burning velocity

For the burning velocity measurements, the ITV schlieren setup from Figure 2- 3 is used in this project. The setup consists of a spherical combustion chamber with an inner diameter of 100 mm. The outer region of the propagating flame is imaged using a Schlieren setup with two field lenses. A pulsed high power LED emitting green light is used together with a high-speed CMOS camera. Images are captured with acquisition rates up to 100,000 frames per second and a resolution of more than 10 pixels per mm. The optical system, which will henceforth be referred to as the optical method, includes an aspherical condenser lens, three spherical lenses, and two pinholes. The images were corrected for lens deforming effects during post-processing.

The mixture is prepared in a separate 1.35 L vessel using the partial pressure method. After evacuation of the combustion vessel and the tube network from residual gases using a separate vacuum pump, the fuel-air mixture is fed from the premixing tank into the combustion chamber and the desired initial condition p_0, T_0 is set. After sufficient resting time and once the set-point ignition pressure remains steady, the mixture is centrally ignited by a two-step coil and capacitor ignition system, providing spark energies up to 5 J. The spark is discharged via extended spark plug electrodes with diameters of 1 mm and a gap of 2 mm between the electrode tips.

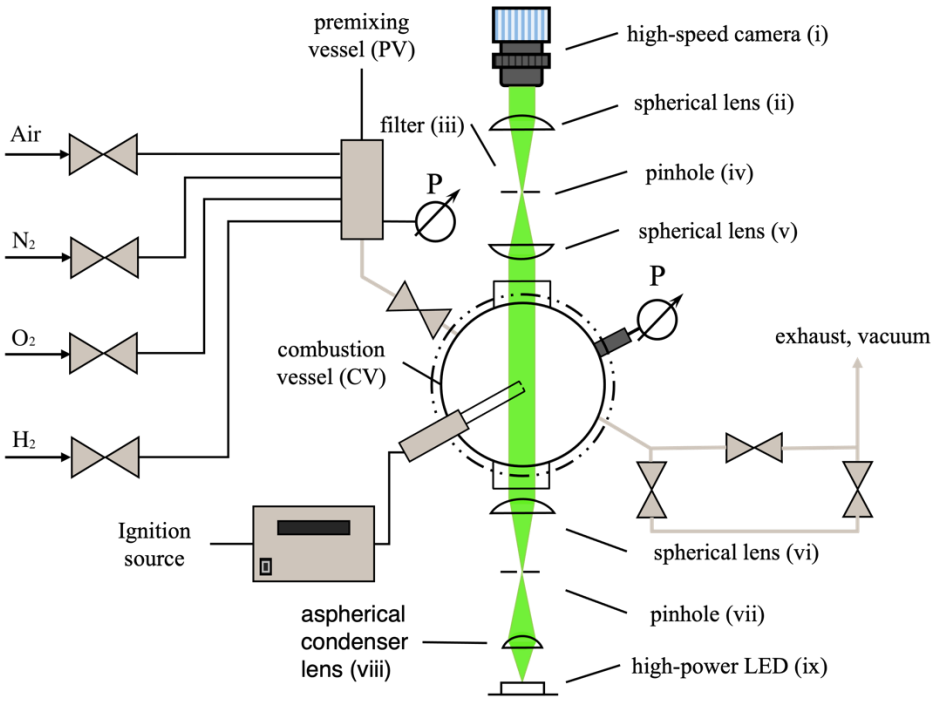

Figure 2- 3 Experimental setup for flame burning velocity measurements.

In common, the stretched propagation speed with respect to the burnt mixture s_b can be determined by the derivative $\mathrm{d}rf/\mathrm{d}t$. The flame stretch rate κ is defined as the temporal change of a flame surface area A [33]. In case of an outwardly expanding spherical flame front, κ can be expressed as

$$\kappa = \frac{1}{A}\frac{dA}{dt} = \frac{2}{r}\frac{drf}{dt}. \quad (2\text{- }1)$$

The response of flames to weak stretch has been analysed on the basis of asymptotic theory. The burnt gas Markstein length L_b can be described as

$$s_b^0 - s_b = \mathcal{L}_b \kappa, \quad (2\text{- }2)$$

where s_b^0 is the unstretched laminar burning velocity with respect to the burnt mixture (hereafter referred to as the linear method, LM) [34].

Apart from LM, additional extrapolation techniques have been proposed to capture the nonlinear behaviour for various reasons. The first reason is the non-linear behaviour of small flames at high stretch rate. Secondly, non-linear effects occur at low stretch for large flames with Lewis numbers significantly away from unity. These effects were discussed for varying fuels, e.g., hydrogen, methane, and *n*-heptane, especially for very lean/rich mixtures at ambient conditions [35].

Besides LM, in the present study, a common non-linear model is utilised to extract s_b^0 and $\mathcal{L}_b$, hereafter referred to as the non-linear method (NM). This technique has been discussed by Halter et al. [36] and is given as

$$\left(\frac{s_b}{s_b^0}\right)^2 \ln\left(\frac{s_b}{s_b^0}\right)^2 = -\frac{2\mathcal{L}_b\kappa}{s_b^0}. \quad (2\text{- }3)$$

It is based on an earlier work of Ronney and Sivashinsky [37]. A least-squares fit is applied to obtain the unknown parameters, s_b^0 and $\mathcal{L}_b$ for LM and NM. For completeness, Kelley and Law [38] proposed a slightly more accurate method for NM using an analytical solution based only on the temporal evolution of the flame radius. Chen [39] showed by data analysis from 1D spherically expanding flame simulations that depending on the mixture Lewis number, either NM for small or a non-linear model proposed by Frankel and Sivanshinsky [40] for large Lewis numbers is favoured. The latter model, under the assumption of large flame radii, shows a linear change with flame curvature. Kelley et al. [41] relaxed the quasi-steady assumption of Eq.

(2- 3). They incorporated an unsteady term already noted by Ronney and Sivashinsky [38] in form of an expansion. Recognising that differences among the aforementioned models start from the second-order inverse power of r_f, Wu et al. [42] proposed an extrapolation equation with a free parameter on the second-order term, which relies on experimental data to describe the curvature. Liang et al. [43] identified the important role of finite flame thickness on highly stretched flames. They adopted the finite flame thickness δ^0 expression into the extrapolation. This is similar to Eq. (2- 3), except for an additional term corresponding to the finite flame thickness.

[1] Frankel and Sivashinsky: $\frac{s_b}{s_b^0} = 1 - \mathcal{L}_b \frac{2}{r_f}$ (2- 4)

[2] Kelley et al.: $\frac{s_b}{s_b^0}\left[1 + \frac{2\mathcal{L}_b}{r_f} + \frac{4\mathcal{L}_b^2}{r_f^2} + \frac{16\mathcal{L}_b^3}{3r_f^3} + o^5\left(\frac{\mathcal{L}_b}{r_f}\right)\right] = 1$ (2- 5)

[3] Wu et al.: $\frac{s_b}{s_b^0} = 1 - \frac{2\mathcal{L}_b}{r_f} + \frac{C}{r_f^2}$ (2- 6)

[4] Liang et al.: $\left(\frac{s_b}{s_b^0} + \frac{2\delta^0}{r_f}\right) \ln\left(\frac{s_b}{s_b^0} + \frac{2\delta^0}{r_f}\right) = -\frac{2(\mathcal{L}_b - \delta^0)}{r_f}$ (2- 7)

Finally, the unstretched laminar burning velocity in the unburned, denoted by s_L , is obtained by applying mass conservation:

$$s_L = \rho_b / \rho_u s_b^0 \quad (2\text{- }8)$$

The densities in burned ρ_b and unburned ρ_u are obtained from equilibrium calculations.

2.2.2 Simulation method for laminar burning velocity

The following governing equations describe unstretched laminar premixed steady flames:

$$\frac{\mathrm{d}\rho v}{\mathrm{d}y} = 0, \quad (2\text{- }9)$$

$$\rho v \frac{\mathrm{d}Y_k}{\mathrm{d}y} + \frac{\mathrm{d}j_k}{\mathrm{d}y} - \dot{m}_k = 0, \quad k \in \mathcal{S}, \quad (2\text{- }10)$$

$$\rho v c_p \frac{\mathrm{d}T}{\mathrm{d}y} - \frac{\mathrm{d}}{\mathrm{d}y}\left(\lambda \frac{\mathrm{d}T}{\mathrm{d}y}\right) + \dot{q}_\mathrm{R} + \sum_{k\in\mathcal{S}} j_k c_{p,k} \frac{\mathrm{d}T}{\mathrm{d}y} + \sum_{k\in\mathcal{S}} h_k \dot{m}_k = 0. \quad (2\text{- }11)$$

The thermal equation of state for ideal gases is added to this set of differential equations,

$$\rho = \frac{pM}{RT}. \quad (2\text{- }12)$$

In Eqs. (2- 9)–(2- 12), y denotes the independent spatial coordinate, $\mathcal{S} = [1, n_\mathrm{s}]$ is the set of species indices, n_s is the number of species, ρ is the density, v is the velocity, c_p is the mixture-averaged specific heat at constant pressure, T is the temperature, λ is the mixture's thermal conductivity, $\dot{q}_\mathrm{R}$represents the net effect of radiation computed using the assumption of the "optically thin" limit [44] [45] [46], p is the pressure, R is the universal gas constant, and M is the mixture's molar mass. $Y_k, \dot{m}_k, h_k, c_{p,k}$, and j_k are the species mass fraction, the mass-based production rate, the specific enthalpy, the specific heat, and the species flux of species k, respectively. The species fluxes and the thermal conductivity are evaluated with a multi-component transport model [47, 48] model that accounts for the Soret effect. The boundary conditions at the origin, $y = 0$, are

$$\boldsymbol{\rho v}\left(\boldsymbol{Y_k} - \boldsymbol{Y_{k,\mathrm{u}}}\right) + \boldsymbol{j_k} = \boldsymbol{0}, \quad \boldsymbol{k} \in \boldsymbol{\mathcal{S}}, \quad (2\text{- }13)$$

$$\boldsymbol{T} - \boldsymbol{T}_\mathrm{u} = \boldsymbol{0}, \quad (2\text{- }14)$$

and the boundary conditions at the end of the computational domain $y = L_\mathrm{d}$, are

$$\frac{\mathrm{d}\boldsymbol{Y_k}}{\mathrm{d}\boldsymbol{y}} = \boldsymbol{0}, \quad \boldsymbol{k} \in \boldsymbol{\mathcal{S}}, \quad (2\text{- }15)$$

$$\frac{\mathrm{d}\boldsymbol{T}}{\mathrm{d}\boldsymbol{y}} = \boldsymbol{0}, \quad (2\text{- }16)$$

where $Y_{k,u}$ and T_u are the given mass fractions and the temperature of the unburned gas, respectively. L_d must be large enough to ensure vanishingly small derivatives.

The system of non-linear coupled algebraic equations obtained by discretizing Eqs. (2- 9)–(2- 16) was solved in FlameMaster version 4.4.0 [49] employing Newton's method. The simulations used a grid of at least 1000 points, and the numerical results were found to be independent of the grid resolution and the chosen tolerances. The mass flux ρv was determined as an eigenvalue, which was then used to compute the unstretched laminar burning velocity s_L using the density at the origin ($y = 0$).

2.3 Results and discussion

2.3.1 LBV measurements

As reviewed in section 2.1.2.1, H_2 LBV measurements in an O_2-enriched environment are very limited. In this report, measurements for both H_2/Air combustion and oxy-combustion were conducted, and the experimental measurement matrix is shown in Table 2- 5. Regarding oxy-combustion, two O_2 enhanced oxidizers are investigated, namely 35 vol% and 60 vol%, to cover medium and higher O_2 contents. A wide range of equivalence ratios was considered, from 0.5 to 2.5, ranging from lean to rich combustion. Atmospheric, low and high pressures were considered, with a range of 0.5 to 3 bar. All the experiments were performed at an initial temperature of 298 K.

Table 2- 5 H_2 combustion conditions investigated in this work.

O_2 content in the oxidizer (%)	Equivalence ratio	Initial pressure (bar)
21	0.5, 0.8, 1.0, 1.5, 2.0, 2.5	0.5, 1, 3
35	0.5, 0.8, 1.0, 1.5, 2.0, 2.5	0.5, 1, 3
60	0.5, 0.8, 1.0, 1.5, 2.0, 2.5	0.5, 1, 2

For flames in air, images were recorded at 40 kHz, and a square view region was selected to cover the complete flame circle. Figure 2- 4 shows how the spherical flame propagates at different times.

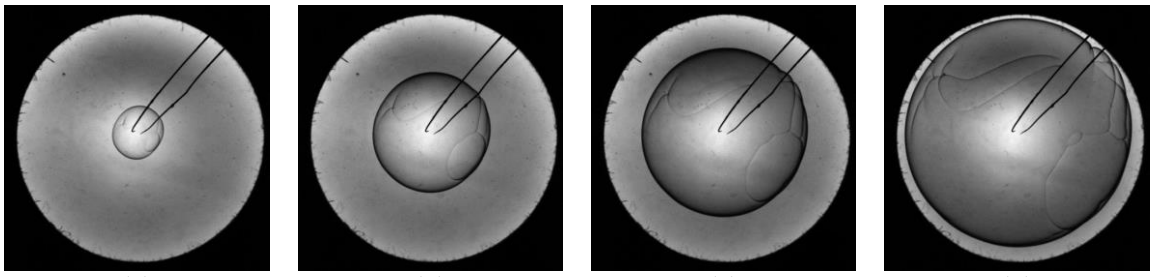

(a) R= 0.27 cm t=0.1 ms | (b) R= 1.15 cm t=0.3 ms | (c) R= 1.55 cm t=0.5 ms | (d) R= 2.15 cm t=0.6 ms

Figure 2- 4 Sequence of Schlieren images from a hydrogen/air flame at standard conditions (298 K, 1 atm) and an equivalence ratio of 1.

At higher oxygen concentrations, as flames propagate faster, field of view was sacrificed to increase the image rate to 100 kHz. The flame radius was extracted in the vertical direction, as shown in Figure 2- 5.

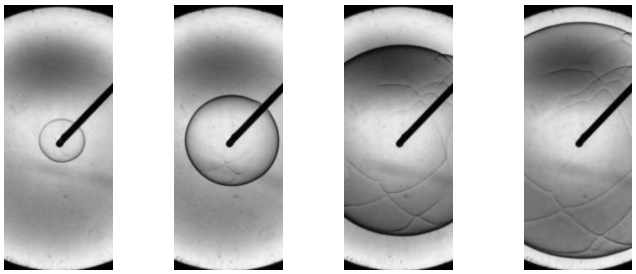

(a) R= 0.21 cm t=0.1 ms | (b) R= 0.88 cm t=0.2 ms | (c) R= 1.43 cm t=0.3 ms | (d) R= 2.11 cm t=0.4 ms

Figure 2- 5 Sequence of Schlieren images from a hydrogen flame with an oxidizer O_2/N_2 ratio of 60/40. Initial conditions are 298 K and 1 atm and an equivalence ratio of 1.

The measured LVB of H_2 under various equivalence ratios are presented in Figure 2- 6, and the effects of O_2 content in the oxidizer and initial pressure are displayed in Figure 2- 6 (a) and Figure 2- 6 (b), respectively. The laminar burning velocity increases with rising O_2 concentration. At Φ=0.5, raising O_2 content in the oxidizer from 21% to 35% increases the flame speed threefold. Further increase in oxygen content from 35% to 60% increases LBV of H_2 by 2.3. At Φ=1.0, LBV of H_2 at 35% oxygen content is 1.7 times higher than that burning in air, and increasing O_2 content from 35% to 60% leads to another 1.5 times enhancement. On the far rich side, for instance at Φ=2.5, LBV is increased by factors of 1.6 and 1.4 when raising O_2 content from 21% to 35% and 35% to 60%, respectively.

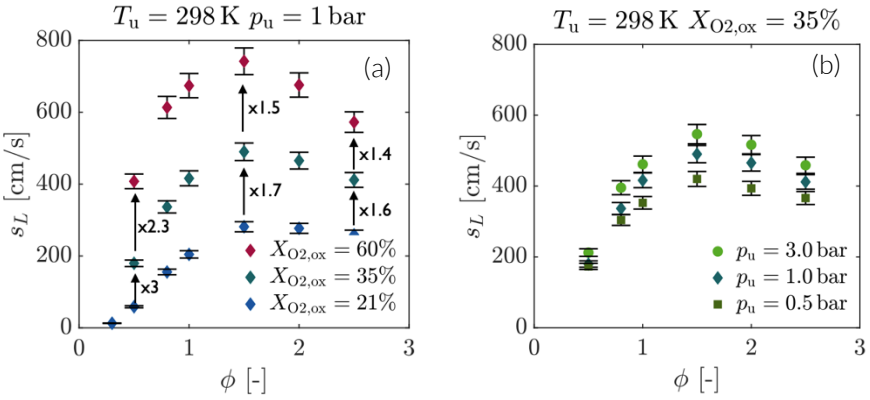

Figure 2- 6 Laminar burning velocity results over equivalence ratio at various oxidizer compositions and different initial pressures. The initial temperature is 298 K.

In addition, stable flames are observed for all measured conditions when the equivalence ratio Φ is greater than 1.5. On one hand, oxygen enrichment in the mixture increases the stability of the propagating flame; on the other hand, an increase of initial pressure reduces the stable flame regime.

2.3.2 H_2/O_2 chemical kinetic model evaluation

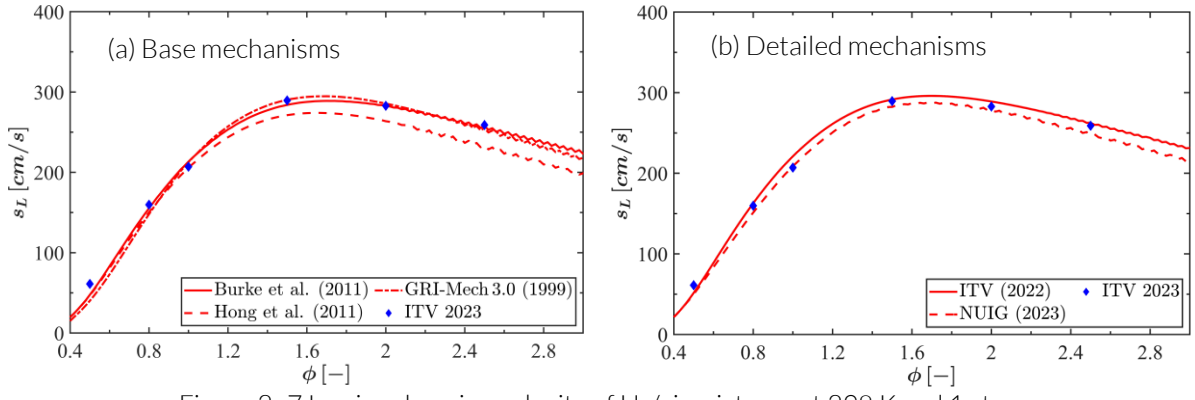

Figure 2- 7 Laminar burning velocity of H_2/air mixtures at 298 K and 1 atm.

The comparison of the numerically determined LBV of the investigated kinetic mechanisms at standard conditions (298 K and 1 atm) shows that for both Burke [19] and GRI-Mech 3.0 [20], there is a very good agreement with the experimental data. Hong [18] model shows an increased underprediction of the LBV with enrichment. In addition, the ITV and NUIG mechanisms exhibit reasonable agreement, although the NUIG slightly underpredicts the data.

A variation in increasing oxygen contents is undertaken to further evaluate the chosen kinetic models' performance. Comparison of experimental data and corresponding computed results is shown in Figure 2- 8. Based on this figure, it can be stated that the basic models increasingly underpredict the experimental LBV with increasing O_2 content, Figure 2- 8 (a), (c), and (e). In particular, it can be seen here, that the GRI-Mech 3.0 [20] predicts higher LBV than Hong [18] and Burke [19], which both show decreasing differences in their predictions with increasing oxygen content. The NUIG mechanism predictions exhibit excellent agreement with the experimental data. As O_2 content increases, the differences between ITV and NUIG predictions increase, with the ITV mechanism increasingly underestimating LBV.

Therefore, the NUIG mechanism is identified as the best-performing model for predicting LBV at standard pressure and temperature, and across oxygen contents.

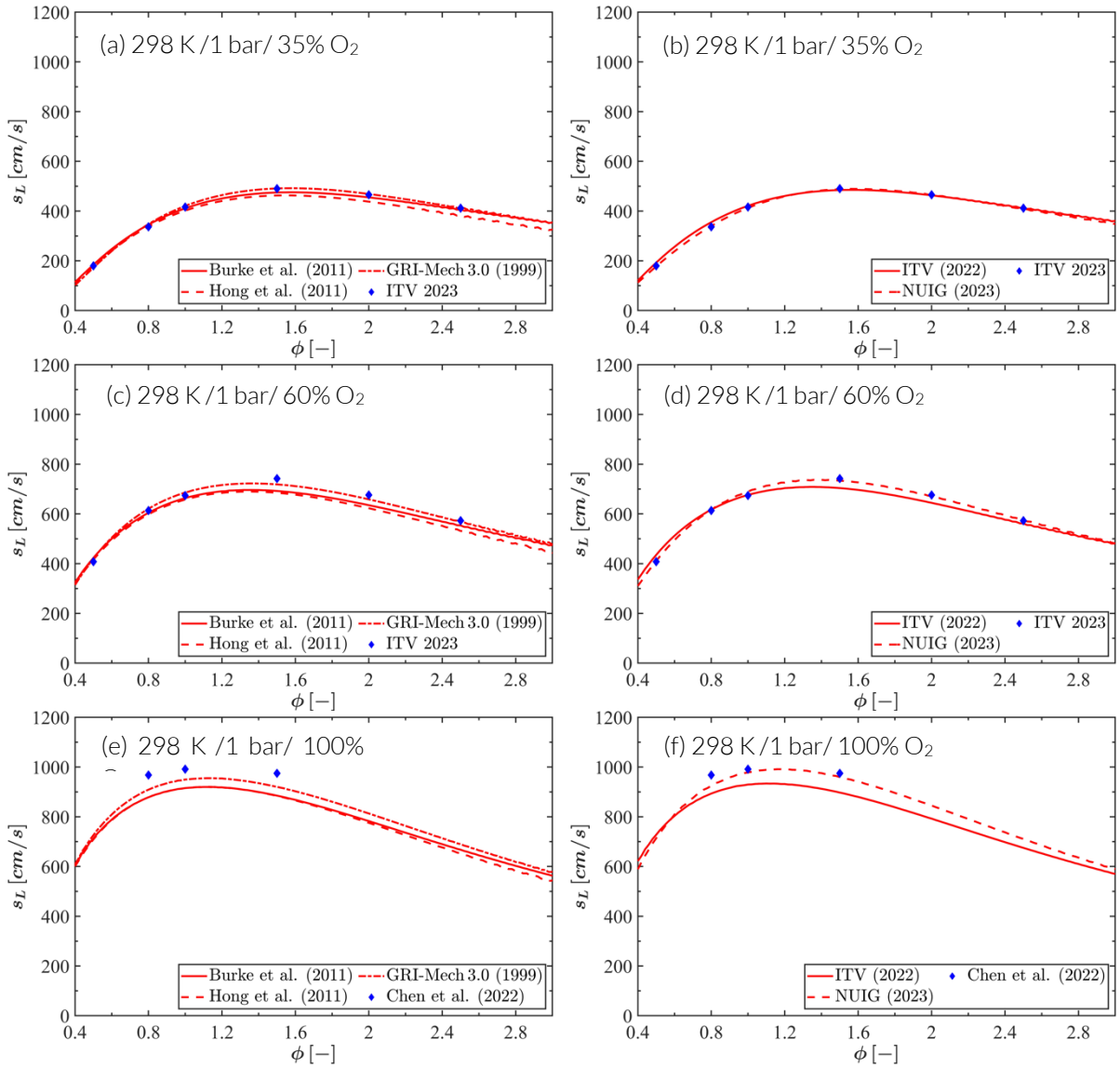

Figure 2- 8 Laminar burning velocities of H_2 burning in with varying O_2 contents at 298 K and 1 atm.

3 Radiation modelling and heat transfer for engineering (RANS) and high-fidelity (LES) simulations

3.1 Introduction

The steel and aluminium industries are high-energy consumers due to their numerous high-temperature processes. These processes usually involve heating materials from room temperature to the required temperature for further processing in the production line. The energy for the heating process comes from fuel combustion in one or multiple burners installed in the furnace. Chemical reactions convert the fuel chemical energy into thermal energy in the high-temperature flue gases. This energy is then transferred inside the furnace through different mechanisms. The flue gases convey energy to the load (heating process) and the furnace walls through convection and radiation. Meanwhile, the heated walls emit radiation toward the furnace interior while some energy is transferred through the walls by conduction and dissipated to the furnace surroundings. The energy reaching the load is spread through conduction, and as the load heats up, it emits radiation back into the furnace. The dominant heat transfer mechanism depends on the temperature of the heating process. Convective heat transfer prevails below 600°C, while radiation becomes predominant above 800°C and may represent over 80% of the total energy transfer to the load for a process temperature over 900°C [50]. Consequently, accurately modelling radiation heat transfer in Computational Fluid Dynamic (CFD) simulations is crucial for correctly designing and evaluating of high-temperature processes.

A description of the models to account for thermal radiation simulations to be carried out in HyInHeat is described next. To choose the most suitable model for LES (Large Eddy Simulations), the models are first applied in the frame of RANS (Reynolds Averaged Navier-Stokes) simulations. Based on the relationship of cost and accuracy for the specific furnaces and burners under study a thermal radiation model will be finally chosen for the LES.

3.2 Radiative heat transfer equation and gas absorptivity

Thermal radiation is a heat transfer mode that consists of the transmission of heat through the propagation of electromagnetic waves or streams of photons. Since such propagation occurs at the speed of light, its transmission can be considered instantaneous with regards to any other phenomenon occurring in the flow, and can even propagate in the vacuum. Therefore, regarding the time scales of the flow, it can be considered that thermal radiation is heat transfer mechanism that transmits energy instantaneously between two distant points.

Radiation shows spatial and directional dependences as well as a strong dependence on the wavelength or wavenumber. Consequently, it hinges on at least six independent variables, namely, three for position, two for direction, plus the wavenumber.

The radiative energy can be absorbed, transmitted, reflected or scattered and emitted. Therefore, considering a surface (for walls) or volume (for fluids) element the ratio of the absorbed, transmitted, reflected or scattered energy with regards to the incident energy allows to define the absorption (κ), transmission (τ), reflection (ρ) or dispersion (σ_s) coefficients, respectively. The sum of the absorption and dispersion coefficients in a fluid is called the extinction coefficient (β). If the extinction coefficient is different to zero then the medium is said to be participating.

With regards to the emitted energy, it is maximum for a black body (a body that absorbs all the radiation it receives) with a spectral dependence described by Planck's law. The ratio of the emitted energy by a (gray) body and a black one at the same temperature is the emissivity ε. It can be shown that emissivity is equal to the absorption coefficient α (Kirchoff's law).

The energy transmitted per unit of time, unit of surface and unit of solid angle in a given direction is called intensity (I). The equation to describe the spatial and directional evolution of the intensity is the Radiative Transfer Equation (RTE), described in the next paragraph.

3.2.1 Radiative transfer equation (RTE)

The Radiative Transfer Equation (RTE) describes the spatial and directional dependence for the intensity $\boldsymbol{I}$. It is obtained from an energetic balance on a differential volume placed at position $\boldsymbol{r}$ along direction $\boldsymbol{s}$:

$$\frac{dI(\mathbf{r},\mathbf{s})}{ds} = \nabla I \cdot \mathbf{s} = \kappa(\xi) I_b(\mathbf{r}) - \kappa(\xi) I(\mathbf{r},\mathbf{s}) - \sigma_s(\xi) I(\mathbf{r},\mathbf{s}) + \frac{\sigma_s(\xi)}{4\pi} \int_{4\pi} I\,(\mathbf{r},\mathbf{s}')\Psi(\mathbf{s},\mathbf{s}')\,d\Omega \qquad (3\text{-}1)$$

where I_b is the black body intensity, κ is the absorption coefficient, σ_s the dispersion coefficient, Ψ the phase function, which describes the ratio of energy redirected from direction $\boldsymbol{s}'$ to $\boldsymbol{s}$, ξ represents the dependence of the coefficients on the thermochemical state of the fluid and Ω is the solid angle. Therefore, the equation states that the variation of intensity is caused by the emission of radiation, minus the absorbed and the out-scattered (usually considered isotropic) intensities plus the in-scattered (which, in general, is considered anisotropic and corresponds to the integral term in the RTE equation) intensity.

It is worth mentioning that the RTE shows, in general, a dependence on the wavenumber. However, such dependence has been deliberately omitted since sometimes a gray gas assumption is considered (assuming constant coefficients in the wavenumber direction). Therefore, depending on the hypothesis considered such dependence should be added.

Sometimes a more convenient form for equation Fehler! Verweisquelle konnte nicht gefunden werden. is obtained if it is written using the dimensionless optical thickness defined as

$$\tau = \int_0^l \beta dl \qquad (3\text{-}2)$$

what leads to the following very compact form of the RTE equation:

$$\frac{\partial I(\mathbf{r_0}+\tau\mathbf{s},\mathbf{s})}{\partial \tau} + I(\mathbf{r_0}+\tau\mathbf{s},\mathbf{s}) = S_\tau(\mathbf{r_0}+\tau\mathbf{s}) \qquad (3\text{-}3)$$

In previous equation the source term values

$$S_\tau(\mathbf{r_0}+\tau\mathbf{s}) = (1-\omega) I_b(\mathbf{r_0}+\tau\mathbf{s}) + \frac{\omega}{4\pi}\int_{4\pi} I\,(\mathbf{r_0}+\tau\mathbf{s},\mathbf{s}')\Psi(\mathbf{s},\mathbf{s}')d\Omega \qquad (3\text{-}4)$$

where ω is the albedo defined as the ratio between the dispersion and extinction coefficients.

In order to solve the RTE a boundary condition has to be given. Depending on the case, different boundary conditions can be given but one of the most usual is considering that walls are opaque (no transmission) and diffusely emitting and reflecting. In that case the boundary condition takes the form

$$I(\mathbf{r_0},\mathbf{s}) = \frac{\kappa(\mathbf{r_0})\sigma_B}{\pi} T^4(\mathbf{r_0}) + \frac{1-\kappa(\mathbf{r_0})}{\pi}\int_{\mathbf{n}\cdot\mathbf{s}'>0} I(\mathbf{r_0},\mathbf{s}')\mathbf{s}'\cdot\mathbf{n}\,d\Omega \qquad (3\text{-}5)$$

It is important to note that in the case of combustion when no particles (e.g. soot, pulverized coal) are present, scattering is negligible compared to absorption. Therefore, as natural gas-hydrogen combustion produces almost no particles, the albedo is almost zero and the contribution for the scattering can be neglected which considerably simplifies the RTE due to the complexity involved in the evaluation of the solid angle integral:

$$\frac{dI(\mathbf{r},\mathbf{s})}{ds} = \kappa(\xi) I_b(\mathbf{r}) - \kappa(\xi) I(\mathbf{r},\mathbf{s}) \qquad (3\text{-}6)$$

3.2.2 Connection between the RTE and the energy equation

In order to couple thermal radiation with the rest of variables of the fluid the net flux of heat due to radiation has to be accounted for in the energy equation. Such flux has to be computed from the intensities. It can be

easily shown that from the knowledge of the intensity and taking its divergence with opposite sign the radiative source term can be computed. Defining the incident intensity as

$$G(\mathbf{r}) = \int_{4\pi} I(\mathbf{r}, \mathbf{s})\, d\Omega \tag{3- 7}$$

it can be shown that the source term that appears in the enthalpy equation takes the form

$$\dot{Q}(\mathbf{r}) = -\nabla \cdot \mathbf{q_r}(\mathbf{r}) = -4\kappa(\mathbf{r})\sigma_B T^4(\mathbf{r}) + \kappa G(\mathbf{r}) \tag{3- 8}$$

This term contributes to the enthalpy equation, which is given by

$$\frac{\partial(\rho h)}{\partial t} + \nabla \cdot (\rho \mathbf{u} h) = -\nabla \cdot \mathbf{F_h} + \frac{\partial p}{\partial t} + \mathbf{u} \cdot \nabla p + \tau : \nabla \mathbf{u} + \dot{Q} \tag{3- 9}$$

where h is the specific enthalpy, ρ is the density, $\boldsymbol{u}$ the velocity, p the pressure, τ the shear stress tensor and F_h the enthalpy diffusive flux.

3.3 Review of radiation heat transfer models

When including radiation heat transfer in a CFD simulation, two main aspects must be considered. First, the method used to solve the RTE or account for its effects; second, the method used to compute the absorption coefficient (κ of the gas mixture). These two aspects are the focus of this and the next section. First, the description of the models to solve the RTE is given. Due to the complexity of integrating the RTE there exists a wide range of models with different levels of accuracy and cost.

3.3.1 Optical thin assumption model

It is the simplest model and it assumes that the gas optical thickness is very small [44] [45] [46]. Therefore, only emission is considered and absorption and scattering are neglected. This leads to consider that the radiative source term takes the form:

$$\dot{Q} = -\nabla \cdot \mathbf{q_r} = -4\sigma_B\left(\kappa_P T^4 - \kappa_{P,0} T_0^4\right) \tag{3- 10}$$

where κ_P is the Planck's absorption coefficient defined as:

$$\kappa_P = \frac{1}{I_b(T)} \int_0^\infty \kappa_\lambda I_{b,\lambda}(T) d\lambda = \frac{\pi}{\sigma_B T^4} \int_0^\infty \kappa_\lambda I_{b,\lambda}(T) d\lambda \tag{3- 11}$$

and T_0 is taken as the mean or minimum wall temperature. The implementation of the OTA model is straightforward but the model, due to its simplicity, cannot properly gather the effects of radiation (directionality, absorption and dispersion). In particular, it leads to an underestimation of the temperatures of the fluid.

3.3.2 Spherical harmonics method – P1 model

This model is based on projecting the intensity field into the orthogonal basis defined by the spherical harmonics set of functions. Such decomposition is truncated and depending on the order of the last term different approximations can be obtained. The most usual approach is simply to retain the average and first spherical harmonics which leads to write $I(r,s) = \frac{1}{4\pi}(G(r) + 3q_r(r) \cdot s)$, approximation that is called P1. After mathematical manipulation one arrives to an elliptic PDE (partial differential equation) for the incident intensity [51] [52]:

$$\nabla \cdot \left(\frac{1}{3\beta} \nabla G\right) - \kappa G = -4\kappa\sigma_B T^4 \tag{3- 12}$$

It is usually solved imposing Marshak's boundary condition (Robin boundary condition type):

$$\frac{2(2-\kappa)}{3\beta}\nabla G \cdot \mathbf{n} + \kappa G = 4\kappa\sigma_B T_w^4 \qquad (3\text{- }13)$$

The P1-approximation introduces a huge reduction in the computational cost and can partially capture the effects of radiation. Its suitability strongly depends on the problem and it can be said that, in general, it can provide good results in optically thick media when there are not important emission sources at the walls. In other cases, its accuracy can be compromised.

Furthermore, a higher accuracy is obtained when the spherical harmonics series is truncated after three terms, ending with sixteen partial differential equations than can be reduced to six [53]. However, the increase in accuracy over the P1 approximation hardly compensates additional complexity and computational cost.

3.3.3 Discrete ordinate model

The Discrete Ordinates Method (DOM) is a model that can provide a very good accuracy at a reasonable cost compared to the Monte Carlo method (MC, which is usually taken as the reference). Compared to the P1-approximation the DOM is considerably more expensive but it can provide a remarkably higher level of description.

In its standard description, the DOM discretizes the RTE in space according to the Finite Volume Method (FVM) [54]. The method discretizes all the possible directions into a given set of directions and evaluates the integrals in solid angle through numerical quadratures. The specific directions ($\boldsymbol{s_i}$) and weights ($\boldsymbol{w_i}$) are tabulated and are determined in order to fulfil some restrictions which consist of providing the exact integrals for different moments associated to the directions. Consequently, only a set of intensities $\boldsymbol{I_i}$, associated to such directions, are solved following the RTE, which once angular discretization has been considered takes the form:

$$\mathbf{s_i} \cdot \nabla I_i(\mathbf{r}) = \kappa(\mathbf{r}) I_b(\mathbf{r}) - \beta(\mathbf{r}) I_i(\mathbf{r}) + \frac{\sigma_s(\mathbf{r})}{4\pi}\sum_{j=1}^{n} w_j I_j(\mathbf{r}) \Psi(\mathbf{s_i}, \mathbf{s_j}) \qquad i = 1, \dots, n \qquad (3\text{- }14)$$

The accuracy of the DOM depends on the special and angular discretization. The latter is given by the number of angular directions used to discretized each octant ($\mathbf{N_\phi x\, N_\theta}$), which gives the number of additional transport equations that must be solved.

Integration of equation Fehler! Verweisquelle konnte nicht gefunden werden. is usually done sweeping the domain according to the direction related to each of intensities. When FVM is applied in space, equation Fehler! Verweisquelle konnte nicht gefunden werden. is integrated for each cell volume providing a relationship between the intensities at the faces and the centre. Assuming a linear relationship between the values at the faces and the centre (given by the numerical scheme used) and substituting into equation Fehler! Verweisquelle konnte nicht gefunden werden. the values at the downstream faces and the centre can be found from the upstream faces (defined by the corresponding direction). This allows to sweep the domain for each of the directions starting from the knowledge of the intensities at the boundaries. In general, an iterative procedure is required until convergence is obtained for the intensities.

Regarding the implementation it is worth mentioning that as the solution for the intensities are obtained by sweeping the domain this implies that there will be subdomains idle until the upstream subdomains have been swept. Important reductions in time can be achieved by solving all the directions simultaneously [55].

DOM is appropriate for optically thin cases but for high optically thickness it can show a very slow convergence. This can be palliated by explicitly considering the forward scattering (in-scattering in the direction associated to the intensity solved) as part of the transmitted intensity.

Finally, to say that due to the weak coupling between the radiation flux and the flow filed, the set of transport equations for radiation heat transfer do not need to be solve every flow iteration (or time step), which allows reducing the overall computational cost [56].

The DOM shows very high potential due to its ability to solve the intensities accurately and, then, fully incorporating the effects of thermal radiation into simulations while needing a considerably less amount of computational resources compared to Monte Carlo method [57] [58] [59].

3.3.4 Photo Monte Carlo model

The Monte Carlo model employs random ray tracing to simulate the path and interactions of individual photons within a computational domain [60]. It involves generating random numbers based on the radiation physics and energy conservations to determine the direction and location of photon emission, subsequent absorption, transmission, and reflection events in the gas and on the wall surfaces. Statistical sampling accumulates these interactions, enabling the estimation of radiative fluxes and heat transfer rates between surfaces and participating medium. This technique excels in handling complex geometries, non-uniform media, and spectrally dependent properties, making it a powerful tool for predicting radiative heat transfer in intricate systems. However, it is computationally expensive. The accuracy and computational cost of the MC model are given by the number of individual photons consider for the statistical sampling process. Inadequate photon count leads to statistical noise and compromises solution reliability.

The Monte Carlo method is the most powerful tool available to solve the RTE. Nevertheless, its elevated computational cost restricts its practical use to serving as a reference for benchmarking purposes.

3.3.5 Comparison of radiation heat transfer models in the literature

In the literature, some studies have compared and evaluated methods for modelling radiation heat transfer in Computational Fluid Dynamics (CFD) in different scenarios, including the Monte Carlo method, Discrete Ordinates Method, Spherical Harmonics Method (P1 and P3), and the Optically thin assumption amount others. Notably, for steady-state, laminar, natural convection, and radiation in a two-dimensional square enclosure, DOM predictions closely match the MC reference solution, while the P1 approximation consistently yields subpar predictions [61-63]. The DOM demonstrates the best combination of computation cost and accuracy across many cases, with P1 performing poorly in most instances. Similarly, in scenarios involving combined conduction and radiation heat transfer, DOM outperforms P1, which consistently yields poor predictions in the whole range of optical thickness (s). P3 performs well for s = 5 and s = 10 but still deviates significantly from the reference solution for s = 0.1 and s = 1 [63].

In applications like laboratory-scale flames, the effect of radiation heat transfer is small, and the model does not play a significant role in the accurate prediction of the temperature of the flame. Consequently, the optically thin assumption and the P1 model yield similar results than the DOM [64, 65]. In the context of furnace with high optical thickness both the DOM and P1 have exhibited good agreement with the reference data, with DOM performing better near steep temperature gradient [66-68]. Similar conclusions were made in an LES of bluff-body stabilized flames, where P1 and DOM models show minor differences, with the DOM model aligning better with experimental data [69].

In summary, these comparisons in the literature provide insights into the strengths and weaknesses of various radiation heat transfer models in CFD simulations, guiding their selection based on specific application requirements and optical conditions. The P1 model, known for its simplicity, often exhibits a propensity to overestimate radiation, particularly when confronted with directional radiation, low participating or optically thin medium, and in scenarios bounded by hot and cold walls. Although computationally more efficient, the P1 method is sometimes overshadowed by its inaccuracies, as evidenced in various benchmark cases [61, 70]. The Discrete Ordinates Method (DOM) is a preferred alternative, offering speed and accuracy balance, particularly in challenging cases, such as for gas radiation in complex geometries with steep temperature gradients [62, 70].

3.4 Evaluation of radiation heat transfer models for CH_4-H_2-Oxy combustion

According to the literature, the DOM is an RHT model with high accuracy in a wide range of applications, showing good performance in conditions from low to high optical thickness. However, the DOM presents a

higher complexity and computational cost that represents a higher challenge for its implementation in the code for the high-fidelity large eddy simulations compared with other models. Therefore, the selection of the RHT models to be implemented in the LES code is guided by an evaluation of the performance of different RHT models under various gas conditions expected from natural gas–hydrogen blends in both air and oxy-fuel combustion.

The Monte Carlo (MC) model is used as a reference for the accuracy of the different RHT models, while the computational cost is judged based on a reference case without including radiation heat transfer (no Rad). The RHT models compared in the evaluation are, from low to high complexity, the optical thin assumption model (OTA), the first-approximation of the spherical harmonics method (P1), and the discrete ordinate model (DOM), the latter with two solid angle discretization, 2x2 and 4x4.

3.4.1 Numerical setup

The evaluation of the different RHT models is done by comparing their performance in a RANS simulation of a reference high-temperature combustion system available in the IOB laboratory at RWTH Aachen University. The reference combustion system is presented in Figure 3- 1; it consists of a prototype high-velocity burner mounted inside a vertical lab-scale furnace with a cylindrical combustion chamber. A heating process is modelled with the thermal load produced by eight cooling tubes. The cooling tubes have a single-end design with air flowing through the central cavity from top to bottom and then through the annular cavity from bottom to top. Four of the eight cooling tubes are activated, while the others are deactivated. The latter increases the challenge for RHT models due to having surfaces with various temperatures and heat fluxes and a low optical thickness. The optical thickness according to [71] equation is $s = 3.6\frac{V}{A} = 0.3$.

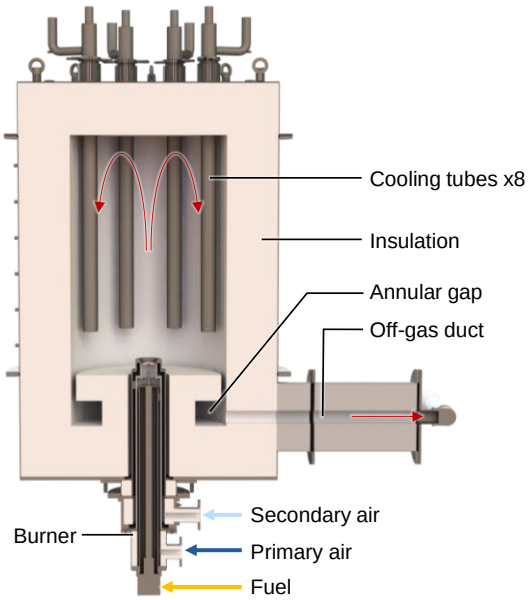

Figure 3- 1 Schematic of the reference high-temperature combustion system.

The geometry of the burner in the combustion system is removed for current simulations, keeping only the nozzle for the injection of hot flue gases into the combustion chamber. This is done to focus on the effect of the RHT model and get rid of the uncertainties in the CH_4-H_2 combustion modelling. A view of the computational domain used in the simulations is shown in Figure 3- 2. Both the fluid region and the solid regions corresponding to the wall insulation and the tubes for the cooling air are included in the simulation. The computational domain is discretized with a structured hexahedral mesh of 1.11 M cells.

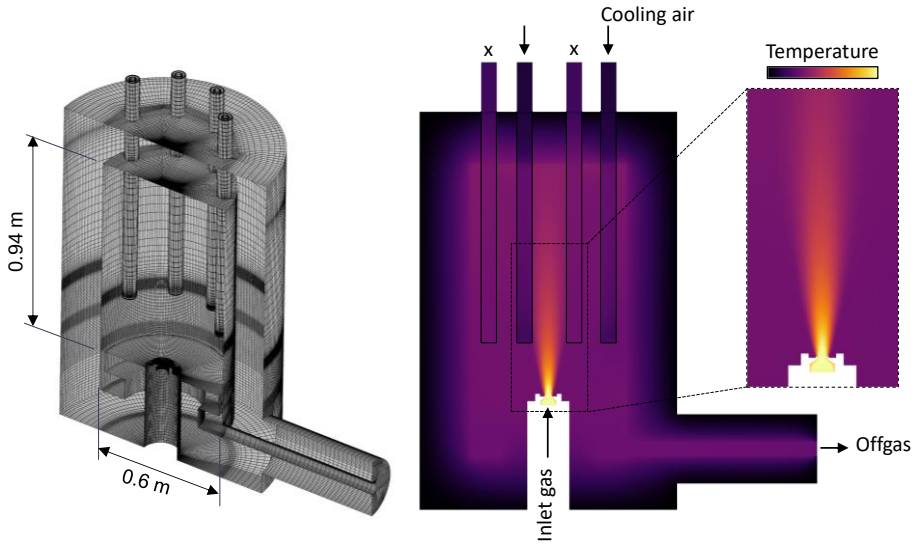

Figure 3- 2 Computational domain for the RANS simulations.

The simulations are done with the double-precision solver based on the pressure of the commercial software ANSYS®-Fluent® version 2023R1. The gases were modelled as a steady-state incompressible Newtonian fluid, and the Reynolds Averaged Navier-Stokes (RANS) equations described the fluid dynamics. The Reynolds stress tensor in the momentum equations is calculated using the Realizable k-**ε** model [72] with the Enhanced Wall Treatment method and considering thermal effects [73] . Pressure-velocity coupling and pressure interpolation are managed with the Couple and PRESTO! [73] are used, respectively. The Second-Order Upwind spatial discretization scheme is used for all the transport equations. Since no combustion is considered, only four species are transported in the simulations: CO_2, H_2O, O_2, and N_2. The energy transport equation is solved in both the fluid and solid regions. The radiation heat flux computed by the various RHT models acts as a source term in the energy transport equation for the fluid region inside the combustion chamber. The gas absorption coefficient was calculated as a function of the local temperature and species composition using the weighted-sum-of-gray-gases model (WSGGM) proposed by [74].

Six conditions are considered for the evaluation of the RHT models, each corresponding to a combination of hydrogen enrichment in the fuel mixture and oxygen in the oxidant. The conditions are summarized in Table 3- 1. Three fuel mixtures with a hydrogen content of 0, 80, and 100% by volume are considered in combination with air and 100% oxygen as oxidants. The composition and temperature of the flue gas used as inlet gas for the simulation considers complete combustion and adiabatic flame temperature. A constant air fuel ratio (one over the equivalence ratio) of 1.15 is taken as a reference.

Table 3- 1 Temperature and mole fraction composition of the flue gas for the CH_4-H_2-Oxy mixtures considered.

Case Name	H_2-Fuel	O_2-Oxi	T [K]	CO_2	H_2O	O_2	N_2
0H21O	0.0	0.21	2100.6	0.084	0.167	0.025	0.724
80H21O	0.8	0.21	2187.7	0.040	0.241	0.024	0.695
100H21O	1.0	0.21	2266.1	0.000	0.309	0.023	0.668
0H100O	0.0	1.0	3030.6	0.303	0.606	0.091	0.000
80H100O	0.8	1.0	3047.4	0.132	0.789	0.079	0.000
100H100O	1.0	1.0	3063.2	0.000	0.930	0.070	0.000

The mass flow rate of the cooling air is 0.013 kg/s for each of the four active tubes. Heat loss through the wall by radiation and convection is computed assuming a natural convection coefficient of 5 W/m^{2}K and an

external emissivity of 0.7. The internal emissivity for the insulation and the surfaces of the cooling pipes equals 0.7.

3.4.2 Results

Radiation heat transfer affects the temperature distribution and the heat flux inside the furnaces. Figure 3-3 shows the gas temperature along the centre axis of the furnaces for the different RHT models and the conditions considered. The case without considering RHT is also included as a reference. In the latter case, the temperature drops from the flame temperature as the inlet gases mix with the recirculating gases that have a lower temperature after transferring heat to the walls by convection. In the cases considering RHT, the temperature drop is more pronounced since the gases transfer heat by radiation to the walls as they are injected into the furnace. The DOM is a perfect match with the MC for both cases with a 2x2 and 4x4 angular discretization. The P1 model tends to overpredict the temperature-drop but is still in good agreement with the DOM and MC. On the other hand, the simple OTA model underpredicts the temperature-drop which results in a temperature profile closer to the case with no RHT, especially when air is used as oxidant. This is explained by the direct dependents of the source term in the OTA model on the average wall temperature. The average wall temperature in the combustion chamber is over 1100 K, resulting in a low radiation heat flux computed by the OTA model.

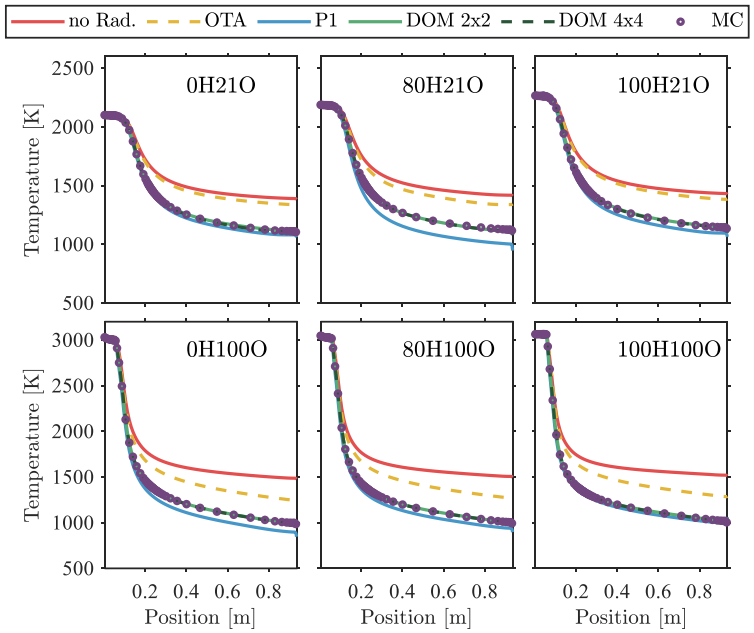

Figure 3- 3 Gas temperature profile along the centre axis of the furnace.

The temperature distribution along the heating tubes is used to evaluate the effect of the RHT model on the heating process. Figure 3- 4 shows the profile of mean temperature along the outer surface of one of the actives cooling tubes. The position is defined with the gas inlet as reference, therefore, the profile goes from bottom to the upper side of the tube. A temperature contour cooling tube is also depicted in Figure 3- 4 for 100H21O. Following the case without RHT as a reference, the temperature distribution presents a steep gradient in the direction of the cooling air flow though the annular gap from bottom to top. When RHT is considered, the temperature along the cooling tubes becomes more homogenous. The DOM agree with the MC while the P1 constantly underpredicts the temperature along the tube for all conditions. The model based on the OTA predicts a temperature distribution far from the reference MC and has a minor effect on the temperature homogeneity. The latter is because the heat radiated by the gases is evenly distributed along all wall surfaces since no transport equation is solve in the OTA, hence, there is not information about the local wall temperature. However, this does not happen with the other models where more heat is transfer to the region with lower temperature.

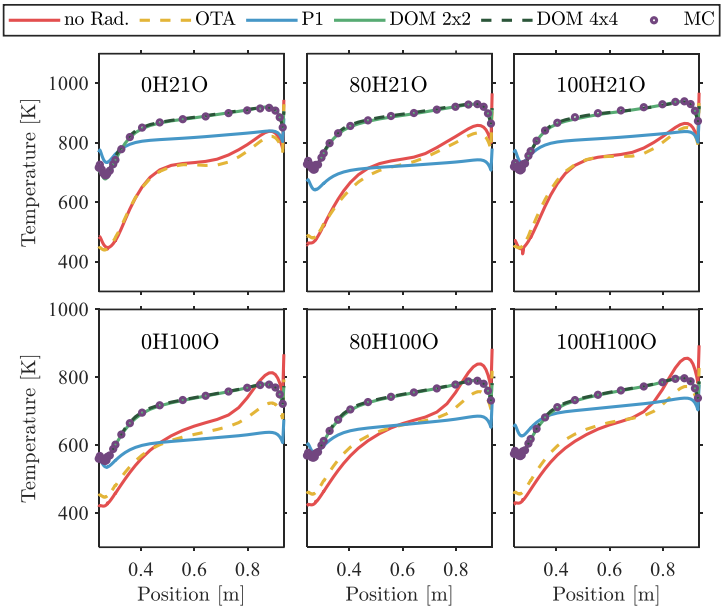

Figure 3- 4 Wall temperature profile along the active cooling tube.

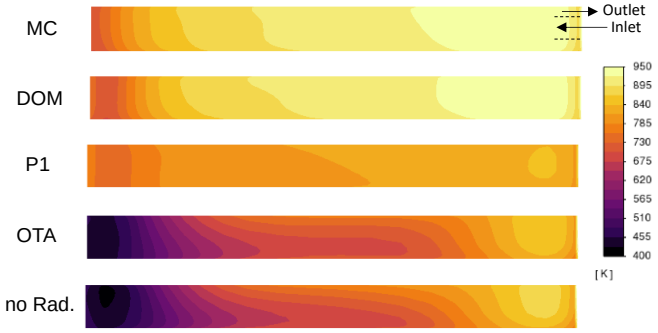

Figure 3- 5 Wall temperature contour cooling tube back face for 100H21O.

The temperature distribution affects the heat transfer by both convection and radiation. The profile of total heat flux along the cooling tube is presented in Figure 3- 6. The P1 model overpredicts the heat flux while the OTA model underpredicts it. The P1 model tends to overpredict radiative fluxes from localized heat sources or sinks [51, 75, 76] as is the case for the cooling tubes. Additionally, this model loses accuracy for small optical thicknesses as in the current test case. The OTA model, on the other hand, underpredicts the heat flux because it only considers heat transfer by radiation from the gases and not from the walls. Radiation heat transfer from the chamber walls to the heating process is a crucial mechanism of heat transfer in the furnace since the surface area of the chamber wall is predominant. The agreement between the DOM and MC is excellent for both 2x2 and 4x4 angular discretization, demonstrating its ability to describe radiation heat transfer in complex applications with high accuracy.

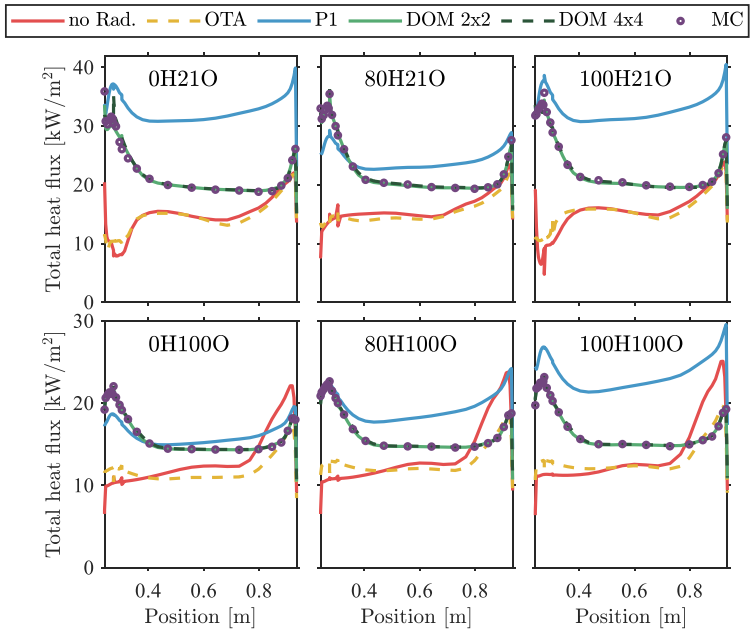

Figure 3- 6 Total heat flux profile along the active cooling tube.

The computational cost of the various RHT models are compared based on the computational cost of the case without considering RHT. Figure 3- 7 shows the Average Time per Iteration (ATI) when running the simulation on ten computer cores. The ATI for the case without RHT corresponds to the computational cost of solving the transport equations for mass, momentum, enthalpy, and species mass fraction. The OTA and P1 models increase the ATI around 10%. The higher increase in the case of the OTA model may be reduced by optimizing the computation of the average wall temperature and the total gas radiation. The ATI with the MC is over 20 times larger than without RHT even when the MC solver is called every 20 iterations, i.e. the coupling between radiation and flow is every 20 iterations. The computational cost of the DOM depends on the angular discretization and the frequency of the radiation and flow coupling. When the RHT is solved every iteration, the ATI is 2.4 and 5 times larger than without RHT for the angular discretization of 2x2 and 4x4, respectively. However, the RHT does not need to be solved every iteration and the computational cost is reduced by increasing the frequency of the radiation and flow coupling. For example, the ATI with the DOM 2x2 is 31% larger than without RHT even the coupling is every 10 iterations.

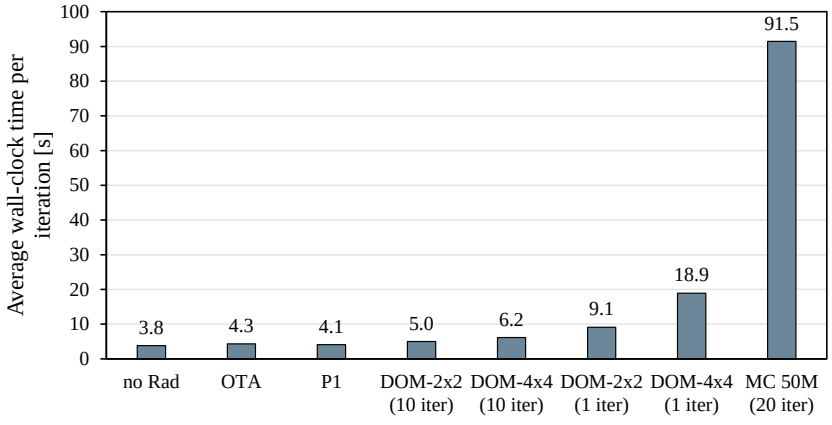

Figure 3- 7 Computational cost performance on ten compute cores.

3.4.3 Conclusion

In conclusion, the evaluation of Radiation Heat Transfer (RHT) models, particularly the P1 and Discrete Ordinate Model (DOM), within the context of Large Eddy Simulations (LES) and Reynolds-averaged Navier-Stokes (RANS) simulations for natural gas-hydrogen (NG-H2) combustion reveals valuable insights. Both models exhibit their strengths and limitations in capturing radiative effects accurately. The P1 model, despite

its simplicity, can sometimes overpredict heat fluxes and temperature drops, potentially due to localized heat source or sink effects and limitations at low optical thicknesses. On the other hand, the DOM demonstrates high accuracy across a wide range of conditions, showing excellent agreement with the Monte Carlo (MC) reference model. While the DOM does introduce higher computational complexity and cost, its performance remains robust and efficient, especially when radiation and flow coupling is optimized. Ultimately, for LES and RANS simulations of NG-H2 combustion, the DOM emerges as a preferable choice due to its balance of accuracy and computational efficiency, making it well-suited for accurate predictions of radiation heat transfer in high-temperature processes involving complex geometries and non-uniform media. Nevertheless, it may be worth implementing the P1 in the LES as an alternative for preliminary calculations due to its low complexity and reasonable accuracy at high optical thicknesses.

3.5 Review of gas radiation models

Gas radiation models differ in their treatment of the spectral dependency of radiative properties. The most accurate treatment of radiation requires to solve the RTE at each wavelength. This is referred to as the Line-by-Line (LBL) approach. Latest spectroscopic databases list more than $\mathbf{10^8}$ spectral lines for H_2O only [77], introducing the same number of transfer equations to be solved. This approach is widely considered far from suitable to employ in engineering applications. Consequently, various models have been proposed, aiming on a computationally cheaper representation of the spectral behaviour [78]. The variety of models ranges from the most detailed LBL models to the simplest assumption of a single gray gas with properties independent of wavelength.

Spectral models reflect the spectral behaviour of radiation, as they use spectral absorption coefficients representing certain wavelength intervals. They are classified into narrow-, and wide-band models, depending on the bandwidth. Band models can be in good agreement with the LBL method at only a fraction of the computational cost. Band models are predestined for cases, where the spectral behaviour of radiation is of interest [78]. Drawbacks of these models are a relatively high complexity when implementing in RTE solvers and a substantial increase of computational cost when applied to combustion CFD simulations, especially for more than one participating species. A computationally cheaper option is provided by global models, where spectral integration is performed before solving the RTE [79].

3.5.1 The Weighted-Sum-of-Gray-Gases Model

The first model following this approach was the weighted-sum-of-gray-gases model (WSGGM) introduced by Hotte and Sarofin [80]. The method consists of substituting the non-gray gas by a set of gray gases for which the heat transfer rates are computed independently. Then the total heat flux is computed through a weighted average of the heat fluxes for each of the gray gases.

Defining the absorptivity as

$$\alpha(T,s) = 1 - e^{\kappa s} \tag{3- 15}$$

where s is the path length and T the temperature, the model assumes that for a mixture of N gray gases the total absorptivity can be written as a sum where each term represents the contribution of each of the gray gases

$$\alpha(T,s) = \sum_{k=0}^{K} a_k(T)(1 - e^{\kappa_k s}) \tag{3- 16}$$

where a_k are tabulated coefficients that fulfill:

$$\sum_{k=0}^{K} a_k(T) = 1 \tag{3-17}$$

It can be shown that for a non-scattering media the gray gases fulfil the equation:

$$\frac{dI_i}{ds} = \kappa_i(a_i I_b - I_i) \quad \text{with} \quad I_i(0) = [a_i I_b](T_w) \tag{3-18}$$

being T_w the wall temperature. The integrated intensity (in wavenumber) for the non-gray gas is approximated as the sum of the intensities solved according to equation (3-18) for each of the gray gases. The coefficients a_k need to be tabulated and they can be obtained from correlations or a minimum square adjustment. A further reduction of computational cost is obtained by a gray implementation, as it is done in many engineering applications and also found in commercial CFD software as Ansys Fluent [73]. Rather than solving N RTEs, the gas is represented by a single gray gas, such that a single RTE needs to be solved. The gray gas absorption coefficient is obtained from the relation:

$$\kappa = -\frac{1}{L} ln(1-\varepsilon) \tag{3-19}$$

with emissivity ε calculated from the weighted sum of gray gases according to equation Fehler! Verweisquelle konnte nicht gefunden werden..

3.5.2 Spectral-Line-Based WSGGM (SLW)

In the SLW model the range of values for the absorption coefficient is partitioned into a set of intervals. New intensities associated to each of such intervals are defined: the RTE for all the wavenumbers whose absorption coefficient is comprised between the limits of one of the previous intervals are added (considering the width in wavenumber). In this way new RTE for intensities related to each of the intervals of the partition are obtained. A geometrical mean $\widetilde{k_i}$ based on the limits of each interval is associated as the representative absorption coefficient for the interval. The RTE equations for these intensities have the form:

$$\frac{dI_i}{ds} = \widetilde{k_i}(T)(\overline{a}_i(T) I_b(T) - I_i) \qquad i = 1, \dots, N \tag{3- 20}$$

where the coefficients $\overline{a}_i$ are tabulated and can be obtained from the knowledge of the black body spectral intensity and the spectral distribution of the absorption coefficient:

$$\overline{a}_i = \frac{1}{I_b} \int_{k_i}^{k_{i+1}} \int_0^{\infty} I_{b\eta}(T) \delta(k - \kappa_\eta)\, d\eta \tag{3- 21}$$

As observed from eq. 3-21 the model is formally identical to the WSGG. Adding the different intensities I_i, the total intensity for the non-gray gas is obtained. As said, the coefficients $\overline{a}_i$ need to be tabulated and they can be obtained from correlations or from integration of the absorption coefficient from detailed databases.

The model was initially developed for non-scattering media surrounded by black walls, but it can be extended to more realistic conditions.

3.5.3 WSGGM for H_2O-CO_2-mixtures

Numerous model formulations and coefficients have been proposed and tabulated, to improve on the accuracy or extent the models' applicability to different scenarios. For applications in gaseous combustion of carbon-based fuels, H_2O, and CO_2 are the essential species determining the radiative participation of the off gas. Consequently, numerous models and coefficients have been proposed and tabulated to describe mixtures of these species. The mixture composition is expressed by the molar ratio of H_2O and CO_2

$$Mr = \frac{X_{\mathrm{H2O}}}{X_{\mathrm{CO2}}} \tag{3-22}$$

and is incorporated into the modelling either by providing different sets of coefficients holding at certain intervals of molar ratios or proposing continuous mathematical formulations depending on the molar ratio Mr.

In literature, a good trade-off between computational cost and accuracy for the prediction of overall radiative heat transfer in the context of combustion is reported [81]. Furthermore, the model can be combined with arbitrary RTE solution methods [60]. This efficiency and flexibility make the WSGGM the most popular model to treat non-gray combustion media [79]. With regard to the project goal of establishing technology in the

industry, the convenient use due to the implementation in commercial CFD software shall be mentioned as well. For these reasons, the WSGGM is chosen for emissivity modelling in CFD simulations of the HyInHeat project. In the following, different WSGGM formulations from literature are compared regarding their ability to cover the combustion scenarios that are expected in the project.

The conditions at which the emissivity models are valid are defined by temperature, pressure path length, and gas composition in terms of radiating species. Hence, it is appropriate to define the conditions of the gas to be modelled in the first step, to identify potential models.

Flue gas temperature is assumed to be bounded within standard temperature $T = 298.15\ K$ at the lower end and the adiabatic flame temperature at the upper end. The adiabatic flame temperature is calculated from the aforementioned equilibrium considerations. For a stoichiometric mixture of pure H_2 and O_2 at standard temperature and atmospheric pressure, a maximum equilibrium temperature of $T_{eq} = 3076.9\ K$ is obtained. The number of molecules passed by a beam of radiation is proportional to pressure and path length. Hence, the quantities are combined to the pressure path length by multiplication. As the demonstrators of HyInHeat typically are operated with a minor pressure excess above ambient pressure, the furnace dimension is the decisive factor. Pressure path length is expected to be well below the bound of $p * s \leq 50$ bar m.

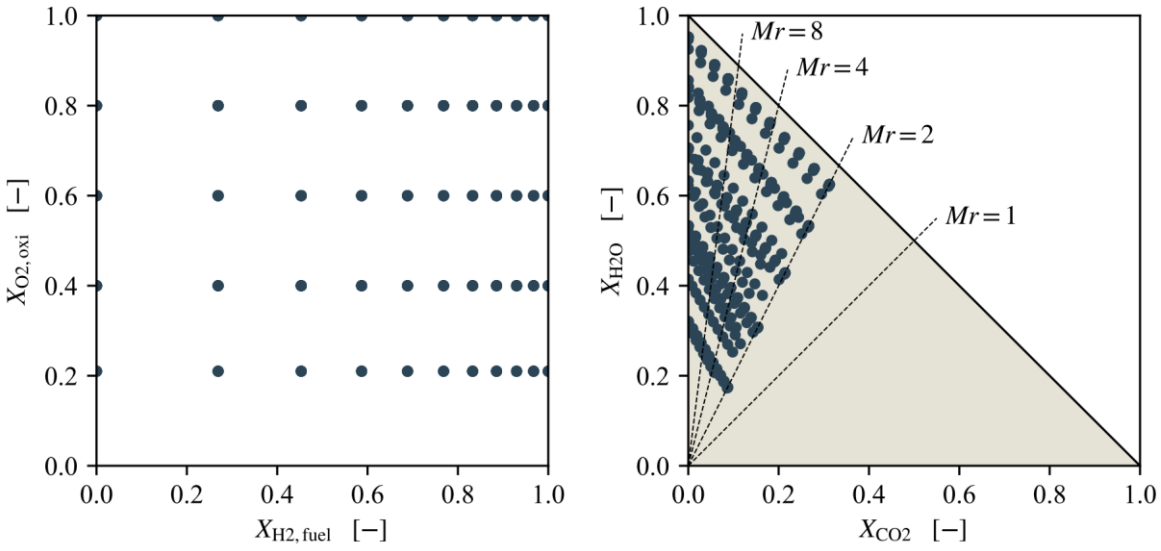

Figure 3- 8 Molar fractions of O_2 in oxidizer and H_2 in fuel (left) and molar ratios of H_2O and CO_2 in flue gas (right).

The most abundant flue gas species are N_2, H_2O, and CO_2, of which only the latter two are considered to take part in radiation. Flue gas compositions are derived from equilibrium calculations at various temperatures, from standard temperature to adiabatic flame temperature. Calculations are done for fuel-oxidant mixtures with oxygen contents of 21% (air), 40%, 60%, 80%, and 100% in the oxidizer and methane/hydrogen fuel blends from 0% to 100% hydrogen enrichment, as shown at the left of Figure 3- 8. The spacing of hydrogen enrichment is chosen in even steps of contribution to the heat of reaction. Resulting flue gas contents of H_2O and CO_2 are shown at the right of Figure 3- 8. The molar ratio, which is used for description of composition in WSGGM, is determined by the combustion stoichiometry. Under stoichiometric conditions of methane combustion, each molecule of methane consumes two molecules of oxygen, producing one molecule of carbon-dioxide and two molecules of water. The molar ratio of the resulting flue gas equals two. Hydrogen enrichment of the fuel alters the reaction, such that the content of CO_2 in the flue gas decreases and the content of H_2O increases. In the case of pure hydrogen combustion, carbon dioxide emissions vanish, and the molar ratio tends towards infinity. Oxygen enrichment and equivalence ratio do not have a direct impact on the molar ratio since they only affect the dilution of the flue gas. Flue gas compositions at different oxygen enrichments are located along a line of constant molar. Slight deviations from these lines are observed at very high temperatures, under which the composition is altered by dissociation into further species as H_2 and CO.

Table 3- 2 Overview of WSGGM for H_2O-CO_2-mixtures.

Authors	n_{gray}	T [K]	Mr	$p * l$ [bar cm]	Reference
Bahador and Sunden [82]	3	500-2500	1-2, Δ	0.1-1000	LBL
Krishnamoorthy [83]	5	1000-2000, Δ	0.5-3, Δ	-	Empirical Corr.
Yin et al. [84]	4	500-3000	0.125-4, Δ	0.1-6000	EWBM
Johansson et al [85]	4	500-2500	0.125-2	0.1-6000	SNBM
Rehfeldt et al. [86]	4	600-2400	0.056-2.167	0.5-5000, Δ	EWBM
Kangwanpongpan et al.[87]	4	400-2500	0.125-2	0.1-6000	LBL
Dorigon et al. [88]	4	400-2500	1-2, Δ	0.1-1000	LBL
Krishnamoorthy [89]	4	-	0.11-2, Δ	-	SNB
Bordbar et al [90]	4	300-2400	0.01-4	1-6000	LBL
Cassol et al. [91]	4	400-2500	0-∞	0.1-1000	LBL
Guo et al.[92]	4	600-2500	0.05-2, Δ	0.1-1000	LBL
Coelho and França [93]	4	400-2500	2	1-12000	LBL
Wang and Xuan [94]	-	500-2500	1	0.01-1000	LBL
Bordbar et al.[74]	4	300-2400	0-∞	1-6000	LBL
Wu et al. [95]	4	400-3000	0.01-4	1-6000	LBL
Xu et al.[96]	5	400-2500	3-∞, Δ	1-90000	LBL

In Table 3- 2, an overview of WSGGM for H_2O–CO_2–mixtures is given by tabulating the number of gray gases n_{gray}, valid ranges of temperature T, molar ratio Mr and pressure path length $p * l$ and the underlying reference models. Authors who published their complete model formulations and coefficients are printed in bold. The letter Δ after a range of values indicates a discrete, rather than continuous model formulation in the respective variable space. While early models used a variety of reference models for calibration, as empirical correlations, Exponential Wide Band Models (EWBM), and Spectral Narrow Band Models (SNBM), latest publications rely on the highly resolved spectroscopic databases and build the models on LBL calculations. Despite a few exceptions, the WSGGM employ four gray gases and hold in a temperature range of $500\ \mathrm{K} < T < 2500\ \mathrm{K}$. All published models are valid for pressure path length up to $10\ \mathrm{bar} \cdot \mathrm{m}$ at least.

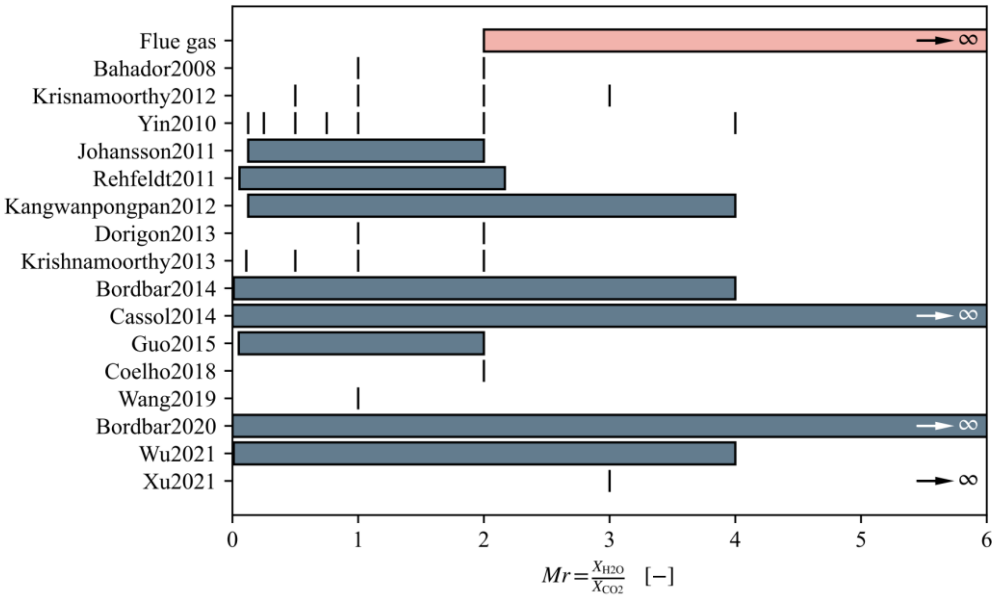

Figure 3- 9 Molar ratio ranges of WSGGM.

The greatest limitation is introduced by the range of molar ratios, which is emphasized in Figure 3- 9. The first horizontal bar indicates the region of molar ratios $2 < Mr < \infty$, that need to be covered by a model describing the off gases in all previously described combustion scenarios. Most models do not account for molar ratios higher than four, let alone infinity, which corresponds to H_2O without CO_2. This is attributed to the fact, that efforts have been made on model development for oxyfuel combustion of fossil fuels in the recent past, but not that much on hydrogen fuel. Due to varying fuel and oxidizer enrichments by hydrogen and oxygen, a continuous model formulation is to be preferred over a discrete formulation. The models of Cassol and Bordbar (see Figure 3- 10) fulfil these requirements, while the remaining lack at least one of the desired properties.

The model by Cassol follows a so-called double integration approach. Two sets of gray gas coefficients are calibrated on the pure species, which are combined in the exponential expression as in equation Fehler! Verweisquelle konnte nicht gefunden werden.. According to the species abundance, weights and absorption coefficients are cross-wise multiplied and summed. Such that the effective number of gray gases is increased to a number of 24, when choosing four gray gases per species, increasing the computational cost of the model. The model proposed by Bordbar incorporates the molar ratio as a parameter. Model coefficients are fitted for several constant molar ratios and are expressed as molar ratio polynomials in a second step of fitting. The problem of the molar ratio approaching infinity for vanishing contents of CO_2 is avoided by an interpolation procedure to recover coefficients for pure H_2O. Interpolation is applied for $Mr > 4$.

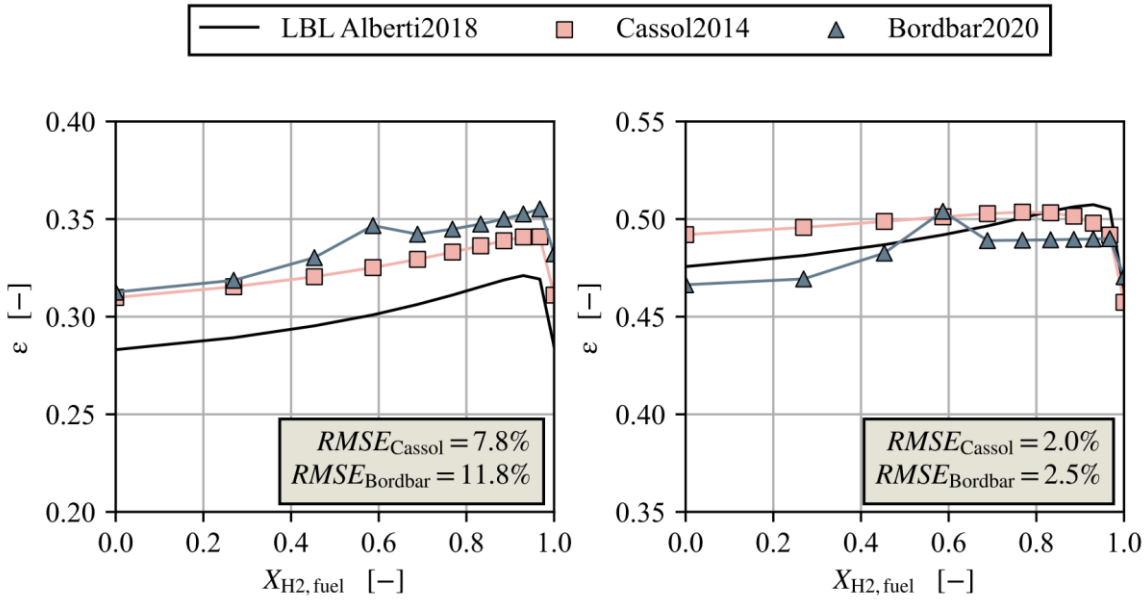

Figure 3- 10 Grey emissivity for air combustion (left) and oxyfuel combustion (right) at varying fuel hydrogen enrichment predicted by WSGGM and LBL calculations.

3.6 WSGGM calibration for CH_4-H_2-Oxy combustion

Since none of the presented models covers the desired range of off-gas conditions, a new model is calibrated to fit the requirements. Tabulated LBL calculations serve as the reference model.

3.6.1 Line-by-line reference

Emissivity is obtained from the LBL calculations tabulated by Alberti [97] considering their latest truncation criterion for the line profiles [98, 99]. Lines are represented by a Lorentz line shape with a resolution of $\Delta\nu = 0.01\ cm^{-1}$ in a spectral range from $\eta_{min} = 0\ cm^{-1}$ to $\eta_{max} = 25.000\ cm^{-1}$.

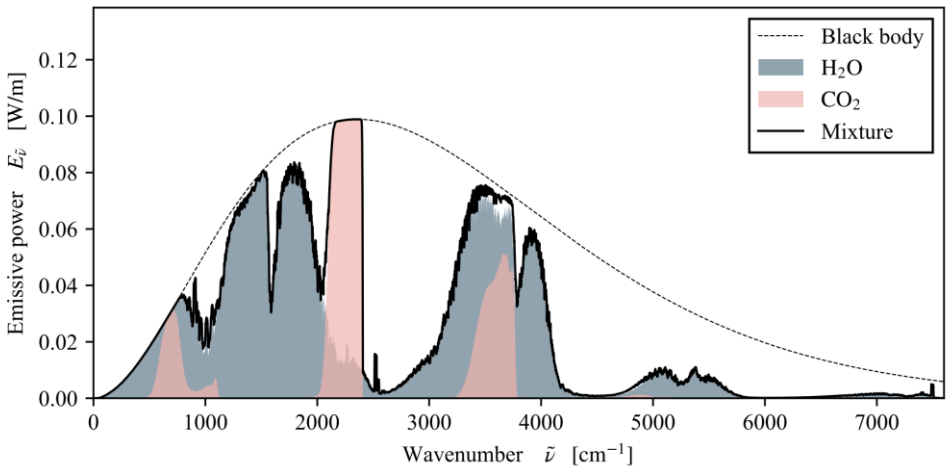

Figure 3- 11 Emissivity spectrum of H_2O-CO_2-mixture at $T = 1770\ K, p = 1.0\ \text{bar}, X_{\text{H2O}} = 43\%, X_{\text{CO2}} = 17\%, X_{\text{N2}} = 40\%$, and $s = 1\ \text{m}$.

A detailed spectrum of an H_2O–CO_2 mixture is shown in Figure 3- 11. The contributions of H_2O and CO_2 are indicated by the coloured regions, the mixtures' spectral emissivity is given by the solid line. The dashed line represents the profile of a black body. The spectral emissivity is condensed into a single gray value by spectral integration of the mixture emissivity and relation to the black body emissivity:

$$\varepsilon_{gray} = \frac{\int_0^\infty [1 - \exp(-\kappa_{\tilde{\nu}} s)] I_{\text{b},\tilde{\nu}}\, \text{d}\tilde{\nu}}{\int_0^\infty I_{\text{b},\tilde{\nu}}\, \text{d}\tilde{\nu}} \tag{3-23}$$

Emissivity is tabulated for arbitrary H_2O-CO_2-CO-N mixtures at temperatures of $300\ \text{K} < T < 3000\ \text{K}$ and pressure path length of $0.005\ \text{bar} \cdot \text{cm} < p \cdot s < 6000\ \text{bar} \cdot \text{cm}$. The tabulated LBL emissivity is evaluated at the conditions given in Table 3- 3:

Table 3- 3 Conditions for WSGGM reference data.

Value	Min.	Max.	Number of points	Spacing
T in K	500	T_{ad}	26	Linear
p in bar	1.01325	1.01325	1	-
$p \cdot s$ in bar $\cdot$ cm	1	6000	20	Different
$X_{\text{O2,oxi}}$	0.21	1	9	Linear
$X_{\text{H2,fuel}}$	0	1	13	Linear in power contribution

The temperature is bounded by the adiabatic flame temperature for each combination of fuel and oxidizer. Evaluated pressure path length in $\text{bar} \cdot \text{cm}$ are 1, 5, 10, 20, 30, 40, 50, 75, 100, 150, 200, 300, 500, 1000, 1500, 2000, 3000, 4000, 5000, 6000. A total of 55.700 emissivities are evaluated and used as reference data for the WSGGM calibration.

3.6.2 WSGGM calibration

The model calibration follows closely the procedure outlined by Bordbar [90]. In agreement with recent literature models, 4 gray gases and a transparent gas are chosen to assure a reasonable trade-off between accuracy and computational cost. In contrast to the conventional WSGGM expression for overall emissivity, a dependency on the molar ratio is introduced to the gray gas weights a_i and absorption coefficients κ_i:

$$\varepsilon = \sum_{i=0}^{I} a_i(T, Mr)\left[1 - e^{-\kappa_i(Mr) ps}\right] \tag{3-24}$$

with the usual restrictions for weights being positive and summing up to unity:

$$a_0 = 1 - \sum_{i=1}^{4} a_i \,, \qquad a_i > 0. \tag{3-25}$$

Weights are expressed as 4th order temperature polynomials. Temperature is related to a reference temperature of $T_{ref} = 1200\ K$, as it is reported to simplify the optimization procedure and increase the model accuracy [84]:

$$a_i = \sum_{j=0}^{4} b_{i,j}(Mr) \left(\frac{T}{T_{ref}}\right)^j \tag{3-26}$$

In the first step, the temperature polynomial coefficients $b_{i,j}$ and the gray gas absorption coefficients are obtained. Equation Fehler! Verweisquelle konnte nicht gefunden werden. is inserted into equation Fehler! Verweisquelle konnte nicht gefunden werden. and the Levenberg-Marquardt method is used, to minimize the Relative Root Mean Squared Error (RMSE) between WSGGM and LBL emissivities. The fitting is performed separately for each constant molar ratio. In this way the molar ratio dependency is evaded in the first step. Each temperature polynomial coefficient and absorption coefficient is in turn expressed as a 4th order polynomial depending on the molar ratio, to account for the mixture composition. At this point, the procedure is altered, compared to Bordbar. As the molar ratio is striving towards infinity for pure hydrogen combustion, the polynomial formulation is not bounded and hence, not suitable to cover this condition. For this reason, the inverse of the molar ratio is chosen, to build the polynomial on:

$$b_{i,j} = \sum_{k=0}^{4} C_{i,j,k}\, Mr^{-k} \tag{3-27}$$

$$\kappa_i = \sum_{k=0}^{4} d_{i,k}\, Mr^{-k} \tag{3-28}$$

The molar ratio coefficients $C_{i,j,k}$ and $d_{i,k}$ are then fitted to recover a continuous formulation for the molar ratio dependency. The fitting of the temperature polynomial coefficients for different molar ratios is shown in Figure 3- 12.

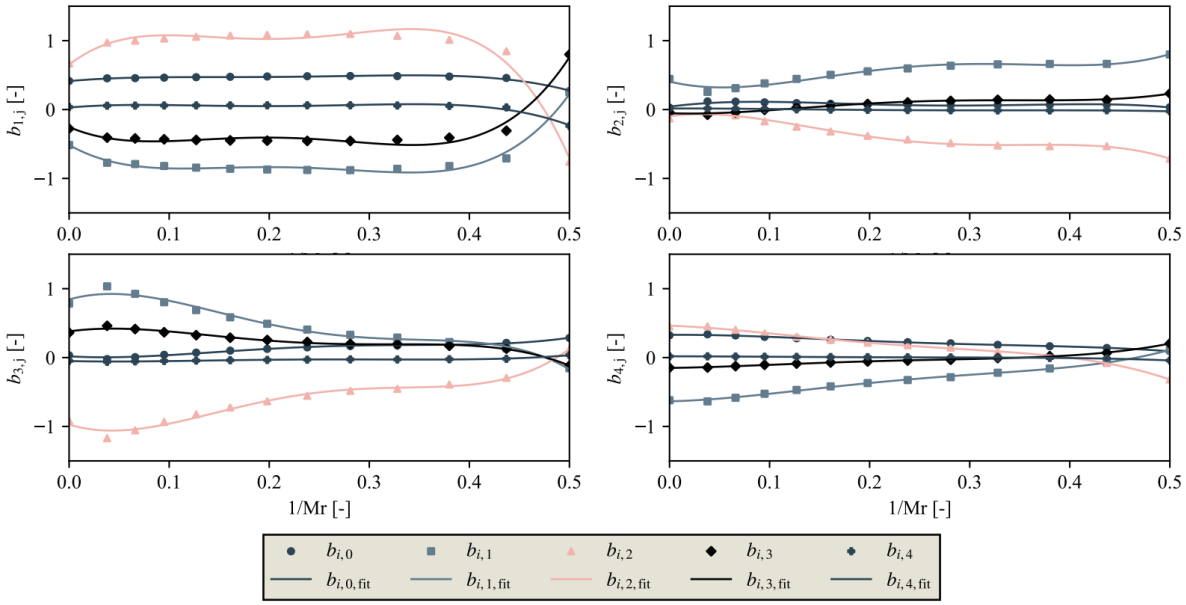

Figure 3- 12 Fitting of WSGGM temperature coefficients on molar ratio.

Fitting of temperature polynomial coefficients on molar ratio is visualized in Figure 3- 12 and fitting of grey gas absorption coefficients on molar ratio is given in Figure 3- 13. It is concluded that 4th order polynomials yield sufficient accuracy in both cases.

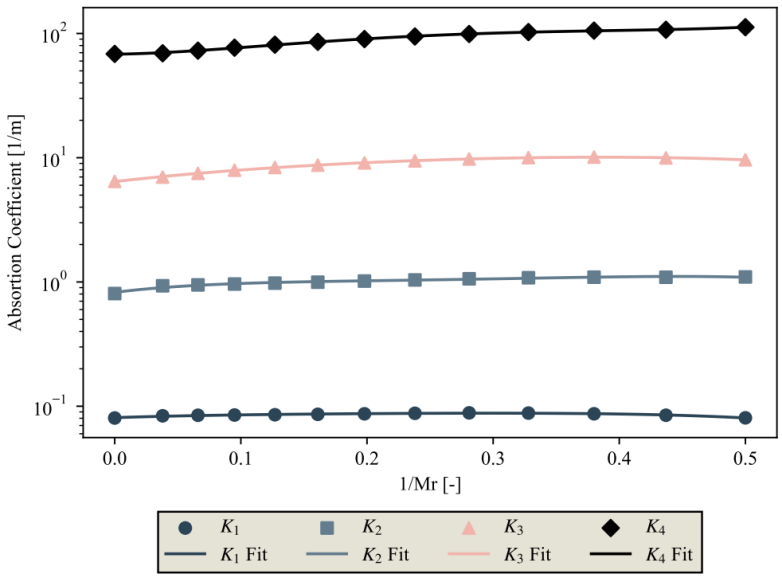

Figure 3- 13 Fitting on WSGGM grey gas absorption coefficients on molar ratio.

3.6.3 Model evaluation: WSGGM vs Line-by-Line

To provide a comprehensive overview of the model's performance, emissivity is evaluated at all data points of the reference data in Figure 3- 14. Each data point is indicating the emissivity from LBL and the corresponding prediction of the WSGGM. The solid line represents an error of zero, meaning the reference and modelled value coincide. The dashed lines indicate the 10% error corridor.

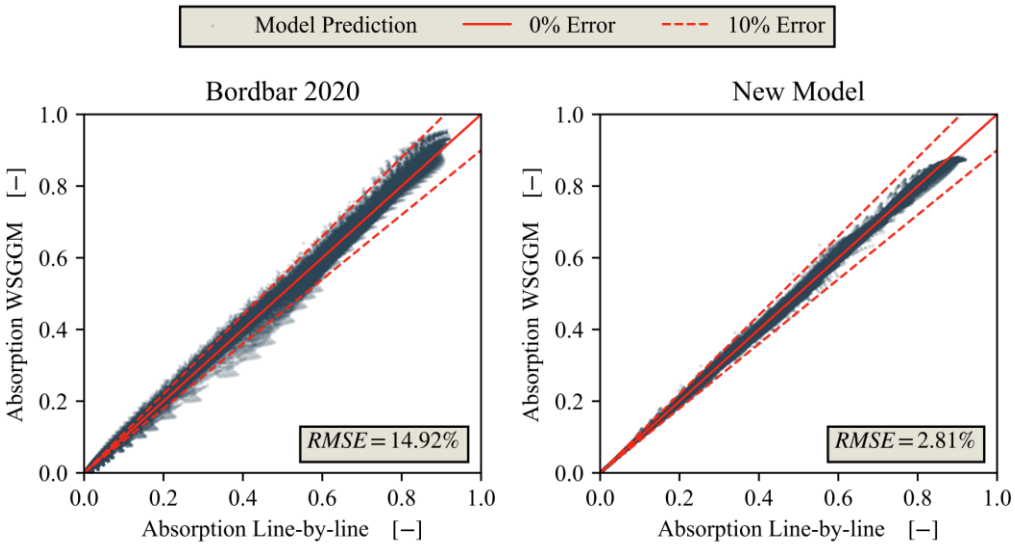

Figure 3- 14 Absorptivity predictions of WSGGM and errors in respect to LBL calculations at optical path length $s = 100\ cm$.

Errors of the bordbar2020 model are attributed to the advancement in LBL procedure as well as the limitation in temperature of $T \leq 2400$ K. Both models suffer errors from the gray gas assumption and the fitting of temperature and molar ratio dependency. A further effect, which is not considered in the model formulations is the self-broadening, which is most significant in the case of H_2O. Higher contents of H_2O introduce a broadening of absorption lines in respect to wavenumber, increasing the gray emissivity due to the wider spectral distribution.

Table 3- 4 RMSE of adjustments to the WSGGM formulation.

Model Version	Adjustment	RMSE
V01	Reference version	2.81%
V02	Increased number of gray gases to $n_{\text{gray}} = 5$	2.96%
V03	Increased Mr-polynomial order to 5 for temperature coefficients $b_{i,j}$	2.57%
V04	Replacement of $\frac{T}{T_{ref}}$ by $ln\left(\frac{T}{T_{ref}}\right)$ for temperature polynomial	2.56%
V05	Combination of V03 and V04	2.47%

Adjustments can be made in the model formulation, to improve the gray emissivity prediction. Options that where investigated are listed in Table 3- 4, where adjustments are listed in relation to the version V01 reference model, which is explained in the previous paragraphs and yields an RMSE of 2.81%. All adjustments add to the computational cost of the model. The most straightforward option is to increase the number of gray gases, which results in decreased errors introduced in the first step of fitting. The obtained coefficients, however, show a higher dependency on molar ratio and cause less accurate fitting in the second step. The overall RMSE is increased to 2.96%. The modification made in the V03 model is to increase the order of the molar ratio polynomial for the temperature coefficients $b_{i,j}$ to 5. The more accurate fitting in the second step reduces the overall error to 2.57%. In model version V04, the temperature polynomial is formulated in terms of the temperature logarithm $ln\left(\frac{T}{T_{ref}}\right)$ rather than the normalized temperature. This adjustment is proposed in a recent WSGGM [96] and reduces the RMSE to 2.56% due to a more accurate representation of the temperature dependency. The combination of measures taken in V03 and V04 yields a RMSE of 2.47%. The choice for a model is up to the user's requirements, at this point it is concluded that none of the modifications could justify the increased computational cost and it is suggested, to use the V01 model for emissivity modelling. Coefficients for the model implementation are given in Table 3- 5:

Table 3- 5 WSGGM coefficients for fitted model.

Coeffcient	i	j	$k=0$	$k=1$	$k=2$	$k=3$	$k=4$
c	1	0	0.462462539	0.239608042	-3.87062089	20.7698399	-30.9364994
c	1	1	-0.747330279	-3.01798267	33.5786764	-140.565798	186.300201
c	1	2	0.874971836	6.36096278	-68.8045312	273.161045	-347.111436
c	1	3	-0.326025047	-4.71376726	52.1070619	-203.874920	254.343771
c	1	4	0.0341765298	1.18487404	-13.3482509	51.9317373	-64.1345762
d	1	-	0.0799741345	0.0801030535	-0.361871790	0.907046828	-1.00043391
c	2	0	0.0671488797	1.32380214	-12.6021052	38.1845194	-37.1182797
c	2	1	0.370035180	-2.69994719	38.0176260	-122.204738	120.859999
c	2	2	-0.0741150990	1.54266487	-34.9726013	119.832990	-122.347304
c	2	3	-0.0573874161	-0.463636713	13.9228387	-49.6790492	51.9787396
c	2	4	0.0150406122	0.06.6120962	-2.03411092	7.37805413	-7.79730590
d	2	-	0.857145026	1.61686597	-6.54195127	15.9644648	-14.9219689
c	3	0	-0.0200542466	0.0301294448	8.68194215	-32.6731362	35.2777248
c	3	1	1.05143515	-66.8515134	-28.1386880	109.997667	-121.438489
c	3	2	-1.19715057	0.690656348	30.3172825	-125.028823	144.234222
c	3	3	0.468259661	-0.006292075	-15.5368429	65.1433655	-77.3780809
c	3	4	-0.0616016389	-0.084880996	3.17118523	-13.1479255	15.8197325
d	3	-	6.12212566	23.4230269	-55.9879124	94.3384205	-96.4501154
c	4	0	0.348123846	-31.0276428	-2.83341056	10.7913858	-11.8610877
c	4	1	-0.681023728	1.37201443	4.35775124	-23.0857509	30.4035408
c	4	2	0.501289972	-1.37348708	-3.82346943	24.7109566	-36.2372831
c	4	3	-0.162484001	0.451759729	2.54278608	-14.8273178	21.7100867
c	4	4	0.0193288746	-0.033447964	-0.697416785	3.51422192	-4.94210538
d	4	-	66.7697055	47.0473372	828.163636	-2845.27072	2728.39276

References

1. Peters, N., *Turbulent combustion. Cambridge, UK: Cambridge University Press.".* 2000.
2. Vázquez, M., et al., *Alya: Multiphysics engineering simulation toward exascale.* Journal of computational science, 2016. **14**: p. 15-27.
3. Iplik, E., M. Adendorff, and D. Muren, *Hydrogen Oxyfuel Combustion for Energy-Intensive Industries*, in *Clean Energy Technologies-Hydrogen and Gasification Processes*. 2022, IntechOpen.
4. Egolfopoulos, F.N., et al., *Advances and challenges in laminar flame experiments and implications for combustion chemistry*. Progress in Energy and Combustion Science, 2014. **43**: p. 36-67.
5. Tse, S.D., D. Zhu, and C.K. Law, *Morphology and burning rates of expanding spherical flames in H_2/O_2/inert mixtures up to 60 atmospheres.* Proceedings of the combustion institute, 2000. **28**(2): p. 1793-1800.
6. Dixon-Lewis, G., *Chemical Mechanism and properties of freely propagating hydrogen-oxygen supported flames.* Arch. Combust.;(Poland), 1984. **4**(4).
7. Zitoun, R. and B. Deshaies, *Burning velocities of rich H_2-O_2 flames under cryogenic conditions.* Combustion and flame, 1997. **109**(3): p. 427-435.
8. Jahn, G., *Der zündvorgang in Gasgemischen*. 2019: Walter de Gruyter GmbH & Co KG.
9. Warnatz, J., *Structure of Freely Propagating and Burner-Stabilized Flames in the H_2-Co-O_2 System.* Berichte Der Bunsen-Gesellschaft-Physical Chemistry Chemical Physics, 1979. **83**(9): p. 950-957.
10. Chen, X., et al., *The characteristics of flame propagation in hydrogen/oxygen mixtures.* International Journal of Hydrogen Energy, 2022. **47**(17): p. 10069-10082.
11. Yang, S., et al., *Laminar flame speeds and kinetic modeling of H_2/O_2/diluent mixtures at sub-atmospheric and elevated pressures.* Proceedings of the Combustion Institute, 2017. **36**(1): p. 491-498.
12. Alekseev, V.A., M. Christensen, and A.A. Konnov, *The effect of temperature on the adiabatic burning velocities of diluted hydrogen flames: A kinetic study using an updated mechanism.* Combustion and Flame, 2015. **162**(5): p. 1884-1898.
13. Dayma, G., F. Halter, and P. Dagaut, *New insights into the peculiar behavior of laminar burning velocities of hydrogen-air flames according to pressure and equivalence ratio.* Combustion and Flame, 2014. **161**(9): p. 2235-2241.
14. Krejci, M.C., et al., *Laminar Flame Speed and Ignition Delay Time Data for the Kinetic Modeling of Hydrogen and Syngas Fuel Blends.* Journal of Engineering for Gas Turbines and Power-Transactions of the Asme, 2013. **135**(2).
15. Kuznetsov, M., et al., *Flammability limits and laminar flame speed of hydrogen-air mixtures at sub-atmospheric pressures.* International Journal of Hydrogen Energy, 2012. **37**(22): p. 17580-17588.
16. Hu, E.J., et al., *Experimental and numerical study on laminar burning velocities and flame instabilities of hydrogen-air mixtures at elevated pressures and temperatures.* International Journal of Hydrogen Energy, 2009. **34**(20): p. 8741-8755.
17. Burke, M.P., et al., *Effect of cylindrical confinement on the determination of laminar flame speeds using outwardly propagating flames.* Combustion and Flame, 2009. **156**(4): p. 771-779.
18. Hong, Z., D.F. Davidson, and R.K. Hanson, *An improved H2/O2 mechanism based on recent shock tube/laser absorption measurements.* Combustion and Flame, 2011. **158**(4): p. 633-644.
19. Burke, M.P., et al., *Comprehensive H_2/O_2 kinetic model for high - pressure combustion.* International Journal of Chemical Kinetics, 2012. **44**(7): p. 444-474.
20. Smith, G.P., et al., *The GRI-Mech 3.0 mechanism.* Univ. of California, Berkeley, 1999.
21. Langer, R., Q. Mao, and H. Pitsch, *A detailed kinetic model for aromatics formation from small hydrocarbon and gasoline surrogate fuel combustion.* Combustion and Flame, 2023. **258**: p. 112574.
22. Sun, H., et al., *High-pressure laminar flame speeds and kinetic modeling of carbon monoxide/hydrogen combustion.* Proceedings of the Combustion Institute, 2007. **31**(1): p. 439-446.
23. Kéromnès, A., et al., *An experimental and detailed chemical kinetic modeling study of hydrogen and syngas mixture oxidation at elevated pressures.* Combustion and Flame, 2013. **160**(6): p. 995-1011.
24. Wiliams, F., *Chemical-kinetic mechanisms for combustion applications. San Diego mechanism web page, mechanical and aerospace engineering (combustion research), University of California at San Diego*. 2015. p. 1884–1898.
25. Varga, T., et al., *Optimization of a hydrogen combustion mechanism using both direct and indirect measurements.* Proceedings of the Combustion Institute, 2015. **35**(1): p. 589-596.
26. Konnov, A.A., *Yet another kinetic mechanism for hydrogen combustion.* Combustion and Flame, 2019. **203**: p. 14-22.

27. Mei, B., et al., *Enhancement of ammonia combustion with partial fuel cracking strategy: Laminar flame propagation and kinetic modeling investigation of $NH_3/H_2/N_2$/air mixtures up to 10 atm*. Combustion and Flame, 2021. **231**: p. 111472.
28. Sun, W., et al., *Further insights into the core mechanism of H_2/CO/NOx reaction system*. Combustion and Flame, 2022. **245**: p. 112308.
29. Wu, Y.T., et al., *Understanding the antagonistic effect of methanol as a component in surrogate fuel models: A case study of methanol/n-heptane mixtures*. Combustion and Flame, 2021. **226**: p. 229-242.
30. Sanchez, A.L. and F.A. Williams, *Recent advances in understanding of flammability characteristics of hydrogen*. Progress in Energy and Combustion Science, 2014. **41**: p. 1-55.
31. Konnov, A.A., *On the role of excited species in hydrogen combustion*. Combustion and Flame, 2015. **162**(10): p. 3755-3772.
32. Dong, S.J., et al., *A new detailed kinetic model for surrogate fuels: C3MechV3.3*. Applications in Energy and Combustion Science, 2022. **9**.
33. Williams, F. *Analytical and numerical methods for investigation of flow fields with chemical reactions, especially related to combustion*. in *Agard Conference Proceedings*. 1975.
34. Matalon, M. and B.J. Matkowsky, *Flames as gasdynamic discontinuities*. Journal of Fluid Mechanics, 1982. **124**: p. 239-259.
35. Beeckmann, J., et al., *Flame propagation speed and Markstein length of spherically expanding flames: Assessment of extrapolation and measurement techniques*. Proceedings of the Combustion Institute, 2019. **37**(2): p. 1521-1528.
36. Halter, F., T. Tahtouh, and C. Mounaim-Rousselle, *Nonlinear effects of stretch on the flame front propagation*. Combustion and Flame, 2010. **157**(10): p. 1825-1832.
37. Ronney, P.D. and G.I. Sivashinsky, *A Theoretical-Study of Propagation and Extinction of Nonsteady Spherical Flame Fronts*. Siam Journal on Applied Mathematics, 1989. **49**(4): p. 1029-1046.
38. Kelley, A.P. and C.K. Law, *Nonlinear effects in the extraction of laminar flame speeds from expanding spherical flames*. Combustion and Flame, 2009. **156**(9): p. 1844-1851.
39. Chen, Z., *On the extraction of laminar flame speed and Markstein length from outwardly propagating spherical flames*. Combustion and Flame, 2011. **158**(2): p. 291-300.
40. Frankel, M.L. and G.I. Sivashinsky, *On Effects Due to Thermal-Expansion and Lewis Number in Spherical Flame Propagation*. Combustion Science and Technology, 1983. **31**(3-4): p. 131-138.
41. Kelley, A.P., J.K. Bechtold, and C.K. Law, *Premixed flame propagation in a confining vessel with weak pressure rise*. Journal of Fluid Mechanics, 2012. **691**: p. 26-51.
42. Wu, F.J., et al., *Uncertainty in stretch extrapolation of laminar flame speed from expanding spherical flames*. Proceedings of the Combustion Institute, 2015. **35**: p. 663-670.
43. Liang, W.K., F.J. Wu, and C.K. Law, *Extrapolation of laminar flame speeds from stretched flames: Role of finite flame thickness*. Proceedings of the Combustion Institute, 2017. **36**(1): p. 1137-1143.
44. Tien, C.L., *Thermal Radiation Properties of Gases*. Advances in Heat Transfer, 1968. **5**: p. 253–324.
45. Barlow, R.S., et al., *Scalar Profiles and NO Formation in Laminar Opposed-Flow Partially Premixed Methane/Air Flames*. Combustion and Flame, 2001. **127**: p. 2102–2118.
46. Gövert, S., et al., *Heat loss prediction of a confined premixed jet flame using a conjugate heat transfer approach*. International Journal of Heat and Mass Transfer, 2017. **107**: p. 882–894.
47. Ern, A. and V. Giovangigli, *Multicomponent transport algorithms*. Vol. 24. 1994: Springer Science & Business Media.
48. Ern, A. and V. Giovangigli, *Fast and accurate multicomponent transport property evaluation*. Journal of Computational Physics, 1995. **120**(1): p. 105-116.
49. H. Pitsch, R.L., *FlameMaster 4.4.0, a computer code for homogeneous combustion and one-dimensional laminar flame calculations*. 2022.
50. W. Trinks, M.H.M., R. A. Shannon, R. J. Reed, and J.R. Garvey, *Industrial furnaces*. 2004: John Wiley & Sons.
51. Sazhin, S.S., et al., *The P-1 model for thermal radiation transfer: advantages and limitations*. Fuel, 1996. **75**(3): p. 289–294.
52. Krishnamoorthy, G., *A computationally efficient P1 radiation model for modern combustion systems utilizing pre-conditioned conjugate gradient methods*. Applied Thermal Engineering, 2017(119): p. 197–206.
53. *09Deshmukh_CTS_P3 Higher-order spherical harmonics to model radiation in direct numerical simulation of turbulent reacting flows*.
54. Chai, J.C., H.S. Lee, and S.V. Patankar, *Finite-Volume Method for Radiation Heat-Transfer*. Journal of Thermophysics and Heat Transfer, 1994. **8**(3): p. 419-425.

55. Colomer, G., et al., *Parallel algorithms for transport sweeps on unstructured meshes*. Journal of Computational Physics, 2013. **232**(1): p. 118–135.
56. Berger, S., et al., *Aerothermal Prediction of an Aeronautical Combustion Chamber Based on the Coupling of Large Eddy Simulation, Solid Conduction and Radiation Solvers*. Asme Turbo Expo: Turbine Technical Conference and Exposition, 2015, Vol 5a, 2015.
57. Bidi, M., R. Hosseini, and M.R.H. Nobari, *Numerical analysis of methane–air combustion considering radiation effect*. Energy Conversion and Management, 2008. **49**(12): p. 3634–3647.
58. Joseph, D., et al., *Discrete Ordinates and Monte Carlo Methods for Radiative Transfer Simulation Applied to Computational Fluid Dynamics Combustion Modeling*. Journal of Heat Transfer, 2009. **131**(5).
59. Gamil, A.A.A., et al., *Assessment of numerical radiation models on the heat transfer of an aero-engine combustion chamber*. Case Studies in Thermal Engineering, 2020. **22**: p. 100772.
60. Modest, M.F., *The Weighted-Sum-of-Gray-Gases Model for Arbitrary Solution Methods in Radiative Transfer*. Journal of Heat Transfer, 1991. **113**(3): p. 650–656.
61. Liu, F., et al., *The impact of radiative heat transfer in combustion processes and its modeling – with a focus on turbulent flames*. Fuel, 2020. **281**: p. 118555.
62. Sun, Y., X. Zhang, and J.R. Howell, *Assessment of different radiative transfer equation solvers for combined natural convection and radiation heat transfer problems*. Journal of Quantitative Spectroscopy and Radiative Transfer, 2017. **194**: p. 31–46.
63. Sun, Y., X. Zhang, and J.R. Howell, *Evaluation of three different radiative transfer equation solvers for combined conduction and radiation heat transfer*. Journal of Quantitative Spectroscopy and Radiative Transfer, 2016. **184**: p. 262–273.
64. Coelho, P.J., O.J. Teerling, and D. Roekaerts, *Spectral radiative effects and turbulence/radiation interaction in a non-luminous turbulent jet diffusion flame*. Combustion and Flame, 2003. **133**(1-2): p. 75–91.
65. Pal, G., et al., *Comparison of accuracy and computational expense of radiation models in simulation of non-premixed turbulent jet flames*. Combustion and Flame, 2015. **162**(6): p. 2487–2495.
66. Habibi, A., B. Merci, and G.J. Heynderickx, *Impact of radiation models in CFD simulations of steam cracking furnaces*. Computers & Chemical Engineering, 2007. **31**(11): p. 1389–1406.
67. Porter, R., et al., *Evaluation of solution methods for radiative heat transfer in gaseous oxy-fuel combustion environments*. Journal of Quantitative Spectroscopy and Radiative Transfer, 2010. **111**(14): p. 2084–2094.
68. Hu, G., et al., *Impact of Radiation Models in Coupled Simulations of Steam Cracking Furnaces and Reactors*. Industrial & Engineering Chemistry Research, 2015. **54**(9): p. 2453–2465.
69. Fureby, C., *Large Eddy Simulation of turbulent reacting flows with conjugate heat transfer and radiative heat transfer*. Proceedings of the Combustion Institute, 2021. **38**(2): p. 3021–3029.
70. Mazumder, S. and S.m.P. Roy, *Modeling Thermal Radiation in Combustion Environments: Progress and Challenges*. Energies, 2023. **16**(10): p. 4250.
71. Siegel, R. and C.M. Spuckler, *Effect of Index of Refraction on Radiation Characteristics in a Heated Absorbing, Emitting, and Scattering Layer*. Journal of Heat Transfer-Transactions of the Asme, 1992. **114**(3): p. 781-784.
72. Shih, T.H., et al., *A New Kappa-Epsilon Eddy Viscosity Model for High Reynolds-Number Turbulent Flows*. Computers & Fluids, 1995. **24**(3): p. 227-238.
73. Ansys, *Fluent Theory Guide 5.3 Modeling Radiation*. 2023.
74. Bordbar, M.H., G.C. Fraga, and S. Hostikka, *An extended weighted-sum-of-gray-gases model to account for all CO_2-H_2O molar fraction ratios in thermal radiation*. International Communications in Heat and Mass Transfer, 2020. **110**: p. 104400.
75. Siegel, R. and J.R. Howell, *Thermal radiation heat transfer, Hemisphere Pub*. Corp., Washing ton DC, 1992.
76. Sazhin, S.S., et al., *The P-1 model for thermal radiation transfer: advantages and limitations*. Fuel, 1996. **75**(3): p. 289-294.
77. Rothman, L.S., et al., *HITEMP, the high-temperature molecular spectroscopic database*. Journal of Quantitative Spectroscopy and Radiative Transfer, 2010. **111**(15): p. 2139–2150.
78. Yadav, R., C. Balaji, and S.P. Venkateshan, *Radiative Heat Transfer in Participating Media*. 2023, Cham: Springer International Publishing. 201.
79. Modest, M.F. and D.C. Haworth, *Radiative Heat Transfer in Turbulent Combustion Systems*. 2016, Cham: Springer International Publishing. 167.
80. Hotte, H.C. and A.F. Sarofin, *Radiative Transfer*. 1967, New-York: McGraw-Hill.

81. Rajhi, M.A., et al., *Evaluation of gas radiation models in CFD modeling of oxy-combustion.* Energy Conversion and Management, 2014. **81**: p. 83–97.
82. Bahador, M. and B. Sunden, *Evaluation of Weighted Sum of Grey Gases Coefficients for Combustion Gases Using Predicted Emissivities From High Resolution Spectroscopic Databases.* Proceedings of ASME Turbo Expo, 2008: p. 1–9.
83. Krishnamoorthy, G., *A new weighted-sum-of-gray-gases model for CO_2–H_2O gas mixtures.* International Communications in Heat and Mass Transfer, 2010. **37**(9): p. 1182–1186.
84. Yin, C., et al., *New Weighted Sum of Gray Gases Model Applicable to Computational Fluid Dynamics (CFD) Modeling of Oxy−Fuel Combustion: Derivation, Validation, and Implementation.* Energy & Fuels, 2010. **24**(12): p. 6275–6282.
85. Johansson, R., et al., *Account for variations in the H_2O to CO_2 molar ratio when modelling gaseous radiative heat transfer with the weighted-sum-of-grey-gases model.* Combustion and Flame, 2011. **158**(5): p. 893–901.
86. Rehfeldt, S., et al., *Modeling of radiative properties of an Oxyfuel atmosphere with a weighted sum of gray gases for variable carbon dioxide and water vapor concentrations.* Energy Procedia, 2011. **4**: p. 980–987.
87. Kangwanpongpan, T., et al., *New correlations for the weighted-sum-of-gray-gases model in oxy-fuel conditions based on HITEMP 2010 database.* International Journal of Heat and Mass Transfer, 2012. **55**(25-26): p. 7419–7433.
88. Dorigon, L.J., et al., *WSGG correlations based on HITEMP2010 for computation of thermal radiation in non-isothermal, non-homogeneous H_2O/CO_2 mixtures.* International Journal of Heat and Mass Transfer, 2013. **64**: p. 863–873.
89. Krishnamoorthy, G., *A new weighted-sum-of-gray-gases model for oxy-combustion scenarios.* International Journal of Energy Research, 2013. **37**(14): p. 1752–1763.
90. Bordbar, M.H., G. Wecel, and T. Hyppänen, *A line by line based weighted sum of gray gases model for inhomogeneous CO_2–H_2O mixture in oxy-fired combustion.* Combustion and Flame, 2014. **161**(9): p. 2435–2445.
91. Cassol, F., et al., *Application of the weighted-sum-of-gray-gases model for media composed of arbitrary concentrations of H_2O, CO_2 and soot.* International Journal of Heat and Mass Transfer, 2014. **79**: p. 796–806.
92. Guo, J., et al., *A full spectrum k-distribution based weighted-sum-of-gray-gases model for oxy-fuel combustion.* International Journal of Heat and Mass Transfer, 2015. **90**: p. 218–226.
93. Coelho, F.R. and F.H.R. França, *WSGG correlations based on HITEMP2010 for gas mixtures of H_2O and CO_2 in high total pressure conditions.* International Journal of Heat and Mass Transfer, 2018. **127**: p. 105–114.
94. Wang, B. and Y. Xuan, *An improved WSGG model for exhaust gases of aero engines within broader ranges of temperature and pressure variations.* International Journal of Heat and Mass Transfer, 2019. **136**: p. 1299–1310.
95. Wu, X., et al., *A new WSGGM considering CO in oxy-fuel combustion: A theoretical calculation and numerical simulation application.* Combustion and Flame, 2021. **227**: p. 443–455.
96. Xu, J., R. Chen, and H. Meng, *WSGG models for radiative heat transfer calculations in hydrogen and hydrogen-mixture flames at various pressures.* International Journal of Hydrogen Energy, 2021. **46**(61): p. 31452–31466.
97. Alberti, M., R. Weber, and M. Mancini, *Gray gas emissivities for H_2O-CO_2-CO-N_2 mixtures.* Journal of Quantitative Spectroscopy and Radiative Transfer, 2018. **219**: p. 274–291.
98. Alberti, M., R. Weber, and M. Mancini, *Re-creating Hottel's emissivity charts for water vapor and extending them to 40 bar pressure using HITEMP-2010 data base.* Combustion and Flame, 2016. **169**: p. 141–153.
99. Alberti, M., R. Weber, and M. Mancini, *Re-creating Hottel's emissivity charts for carbon dioxide and extending them to 40bar pressure using HITEMP-2010 data base.* Combustion and Flame, 2015. **162**(3): p. 597–612.

Get in touch

Website

http://hyinheat.eu/

Email address

info@hyinheat.eu